Assessing improvements in global ocean pCO_2 machine learning reconstructions with Southern Ocean autonomous sampling

Thea H. Heimdal[1], Galen A. McKinley[1], Adrienne J. Sutton[2], Amanda R. Fay[1], Lucas Gloege[3]

[1]Columbia University and Lamont-Doherty Earth Observatory, Palisades, NY, USA

[2]Pacific Marine Environmental Laboratory, National Oceanic and Atmospheric Administration, Seattle, WA, USA

[3]Open Earth Foundation, Marina del Rey, CA, USA

Correspondence to: Thea H. Heimdal (theimdal@ldeo.columbia.edu)

Abstract

The Southern Ocean plays an important role in the exchange of carbon between the atmosphere and oceans, and is a critical region for the ocean uptake of anthropogenic CO_2. However, estimates of the Southern Ocean air-sea CO_2 flux are highly uncertain due to limited data coverage. Increased sampling in winter and across meridional gradients in the Southern Ocean may improve machine learning (ML) reconstructions of global surface ocean pCO_2. Here, we use a Large Ensemble Testbed (LET) of Earth System Models and the pCO_2-Residual reconstruction method to assess improvements in pCO_2 reconstruction fidelity that could be achieved with additional autonomous sampling in the Southern Ocean added to existing Surface Ocean CO_2 Atlas (SOCAT) observations. The LET allows for a robust evaluation of the skill of pCO_2 reconstructions in space and time through comparison to 'model truth'. With only SOCAT sampling, Southern Ocean and global pCO_2 are overestimated, and thus the ocean carbon sink is underestimated. Incorporating Uncrewed Surface Vehicle (USV) sampling increases the spatial and seasonal coverage of observations within the Southern Ocean, leading to a decrease in the overestimation of pCO_2. A modest number of additional observations in southern hemisphere winter and across meridional gradients in the Southern Ocean leads to improvement in reconstruction bias and root-mean squared error (RMSE) by as much as 95 % and 16 %, respectively, as compared to SOCAT sampling alone. Lastly, the large decadal variability of air-sea CO_2 fluxes shown by SOCAT-only sampling may be partially attributable to undersampling of the Southern Ocean.

Deleted: to

Deleted: ly

Deleted: e

Deleted: ,

Deleted: 6

Deleted: 9

Deleted: using

Deleted: ,

1. Introduction

The ocean plays an important role in mitigating climate change by sequestering anthropogenic carbon emissions. From 1850 to 2023, the oceans have removed a total of 180 ± 35 Gt of carbon (Friedlingstein et al., 2023). In order to fully understand the climate impacts from rising emissions, it is essential to accurately quantify the air-sea CO_2 flux and the global ocean carbon sink in space and time. The Surface Ocean CO_2 ATlas (SOCAT; Bakker et al., 2016) is the largest global database of surface ocean CO_2 observations, with data starting in 1957. The main synthesis and gridded products contain over 33 million high-quality direct shipboard measurements of fCO_2 (fugacity of CO_2) with an uncertainty of < 5 µatm (Bakker et al., 2022). However, due to limited resources for ocean observing, limited number of ships/routes, inaccessible regions and unsafe waters, the database covers only about 1% of the global ocean at monthly 1°x1° spatial resolution over the period of 1982-2023, and is highly biased towards the northern hemisphere.

Mapping methods have been developed to estimate full-coverage surface ocean pCO_2 across space and time by extrapolating to global coverage from these sparse SOCAT observations (e.g., Landschützer et al., 2014; Rödenbeck et al., 2015; Gloege et al., 2022; Bennington et al., 2022a,b). Most of these data products utilize machine learning (ML) algorithms to estimate a non-linear function between a suite of driver variables (i.e., sea surface temperature - SST, sea surface salinity - SSS, mixed layer depth - MLD, Chlorophyll - Chl-a, xCO_2 - atmospheric CO_2) and surface ocean pCO_2 (the target variable) where these are co-located. The driver variables are proxies for processes influencing ocean pCO_2. Full-coverage driver variable datasets are then processed through these ML algorithms to produce estimated global full-coverage surface ocean pCO_2. Since the data products rely on pCO_2 observations to estimate functions between the target and driver variables, data sparsity remains a fundamental limitation to this technique.

It has been suggested that targeted sampling from autonomous platforms combined with ships, filling in the state space of pCO_2, represents a path forward to improve surface ocean pCO_2 reconstructions (Bushinsky et al., 2019; Gregor et al., 2019; Gloege et al., 2021; Djeutchouang et al., 2022; Landschützer et al., 2023; Hauck et al., 2023). One major obstacle, however, is that the indirect pCO_2 estimates from floats have high uncertainties (± 11.4 µatm) and may be biased by as much as ~ 4 µatm (Bakker et al., 2016; Williams et al., 2017; Fay et al., 2018; Gray et al., 2018; Sutton et al., 2021; Mackay and Watson 2021; Wu et al 2022). These large uncertainties and biases

Deleted: against
Deleted: Since
Deleted: 7
Deleted: 2
Deleted: Observation-based data products
Deleted: better constrain
Formatted: Highlight
Deleted: in
Deleted: T
Deleted: ;
Deleted: ;
Deleted: ;
Deleted: ;
Deleted: ;
Deleted: train the algorithms and thus produce these relationships…
Formatted: Subscript
Deleted: likely
Formatted: Font: 12 pt
Formatted: Font: 12 pt
Formatted: Font: 12 pt

arise when pCO$_2$ is not measured directly as in the observations included in SOCAT, but is rather estimated using measurements of pH combined with a regression-derived alkalinity estimate (Williams et al., 2017; Gray et al., 2018). SOCAT includes only direct pCO$_2$ observations. Biases and uncertainties may have large impacts on global air-sea CO$_2$ flux estimates, given that the global mean air-sea disequilibrium is only 5-8 µatm (McKinley et al., 2020). It is therefore critical that bias and uncertainty corrections are well-constrained over different oceanic conditions and over time.

Formatted: Font: 12 pt
Formatted: Font: 12 pt
Formatted: Font: 12 pt
Formatted: Font: 12 pt, Subscript
Formatted: Font: 12 pt
Deleted: can

Uncrewed Surface Vehicles (USVs), such as those manufactured and maintained by Saildrone Inc., represent a new type of autonomous platform that can obtain direct pCO$_2$ observations with significantly lower uncertainties compared to other autonomous methods, and equivalent to the highest-quality shipboard measurements contained in SOCAT (± 2 µatm; Sabine et al., 2020; Sutton et al., 2021). Such improvements in sampling are critically important in the undersampled Southern Ocean. This region is fundamental in terms of the ocean's ability to remove carbon from the atmosphere, being responsible for ~ 40% of the global ocean uptake of anthropogenic CO$_2$ (Khatiwala et al., 2009). Improved data coverage in the Southern Ocean represents thus a major opportunity to advance our understanding of the global ocean carbon sink (Lenton et al., 2006, 2013; Takahashi et al., 2009; Monteiro et al., 2015; Gregor et al., 2019; Gray et al., 2018; Mongwe et al., 2018; Bushinsky et al., 2019; Sutton et al., 2021; Long et al., 2021; Mackay et al., 2022; Wu et al., 2022; Landschützer et al., 2023; Hauck et al., 2023). A combination of SOCAT and Saildrone USV observations would include high accuracy data from both the long record and global coverage of ship tracks, and the expanded finer resolution of spatial and seasonal coverage of the poorly sampled Southern Ocean. Importantly, Saildrone USVs are also able to cover the spatial extent and seasonal cycle of the meridional gradients, which has been shown to be critical in order to reduce errors in reconstructing surface ocean pCO$_2$ (Djeutchouang et al., 2022). A combined approach, with autonomous samples such as those obtained from Saildrone USVs, in addition to high-quality observations collected from ships, represents thus a promising solution to improve surface ocean pCO$_2$ ML reconstructions.

Deleted:

Here, we assess to what extent surface ocean pCO$_2$ reconstructions can improve by implementing the pCO$_2$-Residual machine learning (ML) reconstruction (Bennington et al., 2022a) with the combined inputs of SOCAT and Saildrone USV coverage. However, instead of using real-world observations, we sample the target (i.e., surface ocean pCO_2) and driver variables (i.e., SST, SSS, MLD, Chl-a and xCO_2) from our Large Ensemble Testbed (LET) of Earth System Models (ESMs) (e.g., Stamell et al., 2020; Gloege et al., 2021; Bennington et al., 2022a). There are two major benefits of using a testbed compared to actual observations. First, in an ESM, the surface ocean pCO_2 field is provided precisely at all model times and 1°x1° points. Therefore, the pCO_2 reconstructed by the ML algorithm can be robustly evaluated in space and time against a known 'truth' (i.e., 'model truth'). The reconstruction evaluation is thus not limited to the availability of sparse real-world ocean observations. Secondly, a testbed can be used to plan and evaluate the impact of different sampling strategies on the reconstructed pCO_2. It is important to stress that, by using a model testbed, we do not predict real-world surface ocean pCO_2 and air-sea CO_2 fluxes. The goal here is to assess the accuracy with which an ML algorithm can reconstruct the 'model truth' given inputs of samples consistent with real-world data coverage from the SOCAT database and Saildrone USVs.

Deleted: actual

Deleted: known

Deleted: locations

By utilizing the observational coverage of SOCAT and Saildrone USV transects, we assess to what extent the pCO_2-Residual method accurately reconstructs model surface ocean pCO_2 in space and time. We test the impact of two different USV Southern Ocean sampling schemes, the first based on a sampling campaign completed in 2019 (Sutton et al., 2021), and the second on logistically feasible potential future meridional sampling. Additionally, we explore the timing, magnitude, duration and spatial extent of Southern Ocean USV sample additions that most significantly improve the pCO_2 predictions. Combined, the sampling patterns tested here complements previous studies exploring the impact of additional sampling in the Southern Ocean based on idealized full global coverage of floats, and float observations from recent deployments, including the Southern Ocean Carbon and Climate Observations and Modeling (SOCCOM) project, moorings and sailboats (Bushinsky et al., 2019; Denvil-Sommer et al., 2021; Djeutchouang et al., 2022; Hauck et al., 2023; Behncke et al., 2024; Landschützer et al., 2023).

Formatted: Highlight

Formatted: Highlight

2. Methods

2.1 The Large Ensemble Testbed (LET)

In this study, the Large Ensemble Testbed (LET) includes 25 members from three independent initial-condition ensemble models (i.e., CanESM2, CESM-LENS and GFDL-ESM2M; Kay et al., 2015; Rodgers et al., 2015; Fyfe et al., 2017), giving a total of 75 members within the testbed. We do not use the MPI-GE model that was included in the past LET studies because its Southern Ocean pCO_2 seasonality and decadal variability appear to be anomalously large (Gloege et al., 2021; Fay and McKinley, 2021; Bennington et al., 2022a). Each individual Earth System Model (ESM) is an imperfect representation of the actual Earth system, so the multiple Large Ensembles are used to span different model structures and their representation of internal variability. Each ensemble member undergoes the same external forcing (i.e., historical atmospheric CO_2 before 2005 and Representative Concentration Pathway 8.5 through 2016, plus solar and volcanic forcing), but the spread across the ensemble members gives a unique trajectory of the ocean-atmosphere state over time, i.e., a different state of internal variability as well as the difference across models.

Deleted: s

The LET used in this study includes monthly 1°x1° model output from 1982-2016 (Gloege et al., 2021). For each individual ensemble member of the LET, surface ocean pCO_2 and co-located driver variables (i.e., SST, SSS, Chl-a, MLD, xCO_2) were sampled monthly at a 1°x1° resolution, at times and locations equivalent to SOCAT and Saildrone USV observations (**Fig. 1**; Step 1). While the SOCAT observations were sampled from the testbed matching the actual years of sampling, the USV observations were sampled from the testbed starting in 2007 (for ten-year sampling) or 2012 (for five-year sampling) (see **Sect. 2.4**). As our focus is on reconstruction for the open ocean, testbed output for coastal areas, the Arctic Ocean (>79°N) and marginal seas (Hudson Bay, Caspian Sea, Black Sea, Mediterranean Sea, Baltic Sea, Java Sea, Red Sea and Sea of Okhotsk) were removed prior to algorithm processing.

Deleted: year

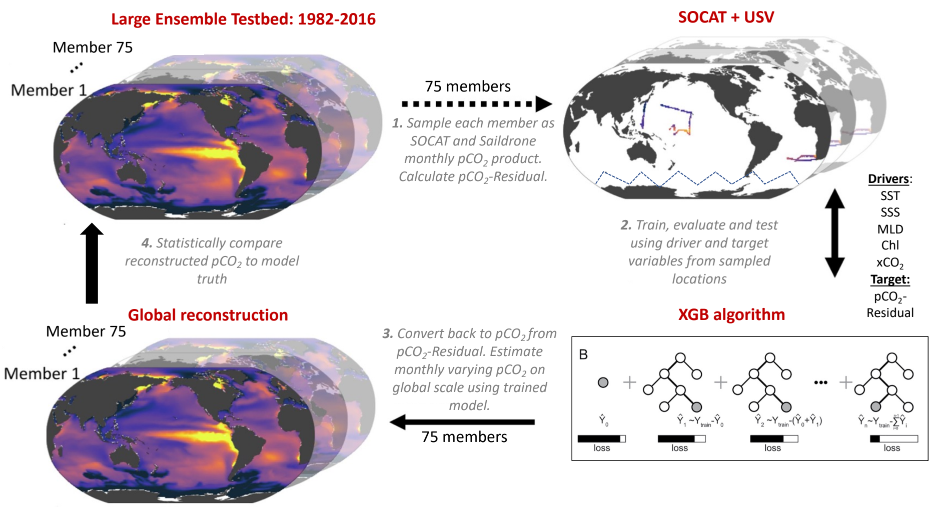

Figure 1: Schematic of the Large Ensemble Testbed (LET; modified from Gloege et al., 2021). **1:** Surface ocean pCO_2 from each of the 75 model members is sampled in space and time mimicking real-world SOCAT and Saildrone USV observations (see **Fig. 2**; **Table 1**; **Section 2.5**). Prior to algorithm processing, pCO_2-Residual is calculated (**Section 2.2**). **2:** The pCO_2-Residual (target variable) and co-located driver variables (i.e., SST, SSS, MLD, Chl, xCO_2) sampled from the testbed are processed by the XGBoost (XGB) algorithm (**Section 2.3**). **3:** Based on the full-coverage of driver variables, pCO_2-Residual is reconstructed globally. This process is repeated 75 times, individually for every single testbed model member. The temperature component (pCO_2-T) is then added back to the pCO_2-Residual for each value. **4:** The globally reconstructed pCO_2 is evaluated against the 'model truth' at all 1°x1° grid cells. SST = sea surface temperature. SSS = sea surface salinity. MLD = mixed layer depth. Chl = chlorophyll. xCO_2 = atmospheric concentration of CO_2.

2.2 The pCO_2-Residual approach

We used the pCO_2-Residual approach following Bennington et al. (2022a), which removes the well-studied direct effect of temperature on pCO_2 from the LET model output before algorithm processing. Temperature has both direct and indirect effects on surface ocean pCO_2. The direct effect of temperature, due to solubility and chemical equilibrium, is that an increase in temperature directly causes an increase in pCO_2 (Takahashi et al., 1993). Indirectly, temperature changes are associated with biological production and wintertime vertical mixing; and these processes tend to result in opposing pCO_2 changes. To build reconstruction algorithms through the data-driven training that occurs in ML, the statistics in all other algorithms developed to date must identify a function that disentangles these competing effects of SST on pCO_2. Here, the algorithm is assisted by removing this known temperature effect, and it must therefore only learn the pCO_2 impacts

Deleted: , i.e., the direct effect of temperature has been removed from the pCO_2 value

Deleted: Since we are using model testbed and not real-world observations, the

Deleted: can

Deleted: be

Deleted: , not just where observations are available

Deleted: ¶

Deleted: prior to

from biogeochemical drivers. The pCO_2-Residual method leads to physically understandable connections between the input data and output (Bennington et al., 2022a), which mitigates to some degree 'black box' concerns typically associated with ML algorithms (Toms et al., 2020). Bennington et al. (2022a) demonstrate higher skill for reconstructions using pCO_2-Residual as the target variable as opposed to pCO_2 (Figure S1 in Bennington et al., 2022a), indicating that the removal of the temperature-driven component enhances the performance of the method. Further, the pCO_2-Residual method has been shown to perform slightly better against independent observations than other common mapping methods (Bennington et al., 2022a). A brief description is provided here, but for further details see Bennington et al. (2022a).

The temperature-driven component of pCO_2 (pCO_2-T) is calculated using this equation:

$$pCO_2\text{-T} = pCO_2^{mean} * \exp[0.0423 * (SST-SST^{mean})]$$

where pCO_2^{mean} and SST^{mean} is the long-term mean of surface ocean pCO_2 and temperature, respectively, using all 1°x1° grid cells from the testbed. Alternative sources of mean pCO_2 were assessed by Bennington et al. (2022a), but they found no significant impact on the test statistics or reconstructed pCO_2. Once pCO_2-T is determined, pCO_2-Residual is calculated as the difference between pCO_2 and the calculated pCO_2-T:

$$pCO_2\text{-Residual} = pCO_2 - pCO_2\text{-T}$$

Prior to algorithm processing, pCO_2-Residual values > 250 µatm and < -250 µatm from the testbed were filtered out targeting values that are not representative of the real ocean. The majority of the pCO_2-Residual values that were filtered out correspond to high pCO_2, above the maximum value in SOCAT (816 µatm; Stamell et al., 2020). The excluded data points (less than 0.2 % per member) mostly occurred in output from the CanESM2 model, and were restricted geographically, predominantly along the western coastline of South America.

The eXtreme Gradient Boosting method (XGB; Chen and Guestrin, 2016) is used to develop an algorithm that allows driver variables (i.e., SST, SSS, Chl-a, MLD, xCO_2) to predict the pCO_2-Residual (**Fig. 1**; Step 2). The pCO_2-Residual and associated feature variables is split into validation, training and testing sets. The test and validation set each account for 20 % of the data, leaving 60 % for training. The validation set is used to optimize the algorithm

Formatted: Highlight
Formatted: Subscript, Highlight
Formatted: Highlight
Formatted: Subscript, Highlight
Formatted: Highlight
Deleted: this
Formatted: Subscript, Highlight
Formatted: Highlight
Formatted: Highlight
Deleted: observation-based products

Formatted: Highlight
Formatted: Font: 12 pt, Not Italic, Highlight
Formatted: Font: 12 pt, Not Italic, Highlight
Formatted: Highlight
Formatted: Font: 12 pt, Not Italic, Highlight
Formatted: Highlight
Formatted: Font: 12 pt, Not Italic, Highlight
Formatted: Font: 12 pt, Not Italic, Highlight
Formatted: Highlight
Formatted: Font: 12 pt, Not Italic, Highlight
Formatted: Highlight
Formatted: Font: 12 pt, Not Italic, Highlight
Formatted: Font: 12 pt, Not Italic, Not Superscript/ Subscript, Highlight
Formatted: Font: 12 pt, Not Italic, Not Superscript/ Subscript
Deleted: to
Deleted: se
Deleted: generally

hyperparameters, which define the architecture of decision trees used in the model. The training set is used to build the decision trees in XGB, while the test set is used to evaluate the performance of the final algorithm. The XGB algorithm for this study used 4,000 decision trees with a maximum depth of 6 levels, and this was fixed for all experiments (see **Supplementary Text A**). For the final reconstruction of surface ocean pCO_2 across all space and time points, the previously calculated pCO_2-T values are added back to the reconstructed pCO_2-Residual (**Fig. 1**; Step 3).

The full XGB process, including 1) training/evaluating/testing and 2) reconstructing globally at a monthly resolution, was repeated individually for each LET member. This process provided therefore a total of 75 unique reconstruction vs. 'model truth' pairs, which can be statistically compared (**Fig. 1**; Step 4).

2.3 Statistical Analysis in the Testbed

The statistical comparisons between the test set and the reconstructions are equivalent to what would be derived using real-world data ('seen' values). Here, we calculate error statistics based on the full reconstruction (pCO_2 from all 1°x1° grid cells of the testbed, except for those masked or filtered out). In the full reconstruction, ~ 99 % of the data do not correspond to SOCAT or Saildrone USV observations used to train the algorithm (**Fig. S1**). Training data would ideally be removed before performance evaluation, but since the training data represent only ~ 1 %, the impact of not removing them is negligible (**Fig. S2**). A suite of statistical metrics can be used to compare the reconstruction to the 'model truth' in order to assess how well the algorithm can extrapolate from sparse data to full-field coverage (**Fig. 1**; Step 4). In this study, we focus on bias and root-mean-squared error (RMSE). Bias is calculated as 'mean prediction – mean observation' (i.e., pCO_2 predicted by XGB subtracted by the pCO_2 'model truth'), and is a measure of over- or underestimation in the reconstructions. RMSE measures the magnitude of the predicted error and is calculated as the square root of the mean of the squared errors. We focus our discussion on the mean across 75 members of the testbed for bias and RMSE. The spread across testbed ensemble members is non-negligible and will be the focus of future work; here, we present the testbed spread primarily in the **Supplement**.

Formatted: Highlight

Formatted: Font: Bold, Highlight

Formatted: Highlight

Formatted: Subscript

Deleted: Since we are using a testbed, we can also include comparisons on additional independent data, referred to as 'unseen' values, which represent the 1°x1° grid cells of the ensemble members that

Formatted: Not Highlight

Deleted:

Formatted: Font: Bold

Formatted: Font: Bold

Formatted: Font: Bold

2.4 Overview of sampling patterns and model runs

First, we sampled target and driver variables from the LET based on sampling distributions equivalent to that of the SOCAT database ('SOCAT-baseline'). Then, we combined the 'SOCAT-baseline' with testbed output representing additional Saildrone USV coverage in the Southern Ocean. The additional Southern Ocean coverage was based on 1) the Sutton et al. (2021) sampling campaign from 2019 ('one-latitude' track) and 2) realistic potential future meridional USV observations ('zigzag' track) (see **Section 2.4.2**; **Fig. 2**). We performed a total of 10 experimental runs (**Table 1**). These represent different sampling approaches, including: 1) repeating USV sampling over a five- or ten-year period, 2) varying the number of USVs and thus the total number of monthly 1°x1° observations, and 3) restricting all observations to southern hemisphere winter months. By comparing the different runs, we can assess whether or not certain targeted sampling strategies in the Southern Ocean can improve surface ocean pCO_2 ML reconstructions. As discussed above, the LET runs to 2016 only (Gloege et al., 2021). Saildrone USV observations were therefore sampled from the testbed starting in year 2006 or 2007 (for the ten-year sampling) or 2012 (for the five-year sampling) until 2016, i.e., the final year of the testbed.

2.4.1 'One-latitude' runs

Six out of the ten experimental runs include the 'one-latitude' track (**Table 1**). The 2019 Saildrone USV journey (Sutton et al., 2021) covered an 8-month period, from January to August. Since the USV was recovered in early August, it did not cover the entire southern hemisphere winter (**Fig. S3**). We repeated this 'one-latitude' eight-month sampling pattern for five years ('5Y_J-A'; 2,075 observations) and ten years ('10Y_J-A'; 4,150 observations). To evaluate year-round ('YR') coverage, the eight-month sampling period (January-August) was shifted by one month each year for ten years ('10Y_YR'; 4,150 observations). To evaluate the impact of increased sampling, the 2019 Saildrone USV track was repeated 12 times with incremental offsets of 1° from the original track, covering an additional 6° north and south (**Fig. S4**). This 'high-sampling'-run ('x13_10Y_J-A'; 44,250 observations) represents a total of 13 USVs. We also performed an additional 13 USV run, but including observations from southern hemisphere winter ('W') months only ('x13_10Y_W'; 25,395 observations). Finally, considering the cost of deploying 13 USVs, a downscaled 'multiple-USV-winter-only'-run was tested, including five USVs sampling over a

Deleted:

Deleted:

Formatted: Font: Bold

Deleted: 1

Deleted:

Deleted: In order t

Deleted: Furthermore, in order t

Deleted: 2

period of five years ('x5_5Y_W'; 5,022 observations). This run covers an additional 2° north and south from the original USV track.

2.4.2 *'Zigzag' runs*

Four of the ten experimental runs represent realistic potential meridional sampling in the Southern Ocean ('zigzag' tracks; **Table 1**) as suggested by Djeutchouang et al. (2022). Saildrone USVs can operate at a speed capable of covering the spatial extent of meridional gradients in the Southern Ocean (Djeutchouang et al., 2022). However, Saildrone USVs are solar powered, and thus their range is restricted by the availability of solar radiation. To account for this and maintain a realistic sampling scenario, sampling occurs only to a maximum latitude of 55° S in these experiments. This alternative sampling pattern represents USVs sailing west to east in a north/south 'zigzag' pattern covering 40° S and 55° S for every 30° of longitude (**Fig. 2**). We created two scenarios. For the first scenario, every 30° of longitude from 40° S and 55° S is visited every three months within a single year as suggested by Lenton et al. (2006). Assuming an average Saildrone USV speed, this scenario represents four platforms equally spaced around the Southern Ocean. This sampling pattern was repeated for 10 years, with year-round coverage ('Zx4_10Y_YR'; 7,600 observations), and for southern hemisphere winter months only ('Zx4_10Y_W'; 2,500 observations). The second scenario represents a 'high-sampling' strategy, where every 30° of longitude from 40° S and 55° S is visited approximately monthly. This can be achieved by deploying 10 platforms equally spaced around the Southern Ocean running at an average Saildrone USV speed. This sampling pattern is repeated for five years, sampling year-round ('Z_x10_5Y_YR'; 11,400 observations) and during southern hemisphere winter months only ('Z_x10_5Y_W'; 3,800 observations).

Formatted: Font: 12 pt, Not Italic

Formatted: Font: 12 pt

Formatted: Font: 12 pt, Not Italic

Deleted: Due to limited solar radiation that powers the Saildrone USVs, we let the sampling occur at a maximum latitude of 55° S.

Deleted: Considering the

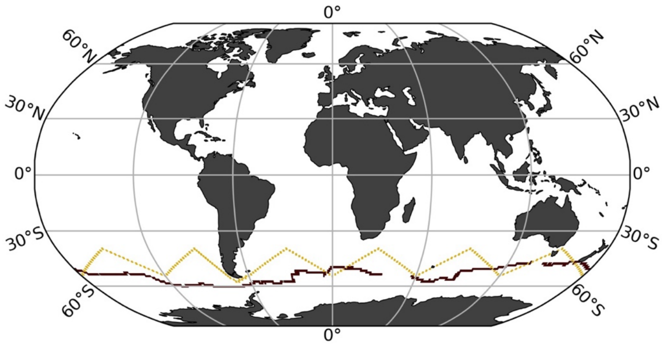

Figure 2: Saildrone Uncrewed Surface Vehicle (USV) tracks representing the first circumnavigation around Antarctica from 2019 in maroon ('one-latitude' track; Sutton et al., 2021) and an alternative virtual route with meridional coverage ('zigzag' track).

Run name	SOCAT-baseline	5Y_J-A	10Y_J-A	10Y_YR	x13_10Y_J-A	x13_10Y_W	x5_5Y_W	Z_x4_10Y_YR	Z_x4_10Y_W	Z_x10_5Y_YR	Z_x10_5Y_W
Saildrone track	NA	One-lat	One-lat	One-lat	One-lat	One-lat	One-lat	Zigzag	Zigzag	Zigzag	Zigzag
Years of sampling	NA	5	10	10	10	10	5	10	10	5	5
Duration of sampling	NA	Jan-Aug	Jan-Aug	Year-round	Jan-Aug	SO winter	SO winter	Year-round	SO winter	Year-round	SO winter
Additional observations	NA	2,075	4,150	4,150	44,250	25,395	5,022	7,600	2,500	11,400	3,800
Global coverage increase (%)	NA	0.01	0.02	0.02	0.3	0.1	0.03	0.04	0.01	0.07	0.02
Mean bias (µatm)											
Testbed period (1982-2016)											
Globally	0.63	0.59	0.59	0.52	0.53	***0.39***	0.57	0.51	0.51	0.45	0.44
NORTH (35°N-90°N)	***0.11***	0.24	0.20	0.25	0.20	0.17	0.16	0.16	0.16	0.12	0.20
MID (35°S-35°N)	0.23	0.21	0.22	0.14	0.20	0.15	0.23	0.20	0.18	***0.13***	0.18
SOUTH (90°S-35°S)	1.4	1.3	1.2	1.1	1.1	***0.80***	1.2	1.1	1.1	1.0	0.87
SO winter months (JJA)	1.3	1.2	1.2	1.1	1.1	***0.90***	1.2	0.93	1.0	0.94	0.95
SO summer months (DJF)	0.070	0.11	0.15	0.10	0.15	***0.019***	0.11	0.25	0.073	0.16	0.066
2006/2012-2016											
Globally	0.51*	0.27	0.34	0.28	0.19	***0.03***	0.21	0.23	0.24	0.17	0.07
SOUTH (90°S-35°S)	1.6*	0.93	1.1	1.0	0.72	***0.37***	0.73	0.89	0.92	0.67	0.55
SOUTH (90°S-35°S) Jun, Jul, Aug	4.2*	2.6	2.7	2.8	2.2	1.8	2.5	1.8	2.4	***1.2***	2.0
Mean RMSE (µatm)											
Testbed period (1982-2016)											
Globally	11.8	11.7	11.8	11.7	11.7	11.6	11.7	***11.5***	11.6	***11.5***	11.6
NORTH (35°N-90°N)	***13.0***	***13.0***	***13.0***	***13.0***	***13.0***	***13.0***	13.1	***13.0***	***13.0***	***13.0***	***13.0***
MID (35°S-35°N)	11.7	11.7	11.7	11.7	11.7	11.7	11.7	11.7	11.7	11.7	11.7
SOUTH (90°S-35°S)	11.5	11.3	11.4	11.2	11.1	11.0	11.3	10.7	11.0	***10.6***	11.0
2006/2012-2016											
Globally	11.6*	11.6	11.4	11.3	11.3	11.2	11.6	***11.0***	11.2	11.1	11.4
SOUTH (90°S-35°S)	11.4*	11.1	11.0	10.7	10.6	10.4	10.9	10.0	10.6	***9.7***	10.6
SOUTH (90°S-35°S) Jun, Jul, Aug	12.0*	11.3	11.2	10.9	10.5	10.3	11.1	10.3	10.6	***9.6***	10.3

Table 1. Overview of the different sampling experiments tested in this study, and mean bias and RMSE (in µatm) for various time periods, latitude bands for all runs. Bold values represent the best score for each category. 'One-lat' = 'one-latitude' track; incorporates the Saildrone USV route from Sutton et al. (2021). 'Zigzag' = potential meridional sampling. 'Additional observations = number of 1°x1° monthly Saildrone USV observations in addition to SOCAT. J-A= January-August. YR = year-round. W = southern hemisphere winter. x4, x5, x10 and x13 = four, five, ten and 13 USVs. SO winter = Southern Ocean winter months, i.e., June, July, August and also including September. *Average value of the mean of 2006-2016 and 2012-2016. The global coverage increase was calculated based on the total number of available 1982-2016 monthly 1°x1° observations from SOCAT (262,204 observations) and the Large Ensemble Testbed (17,290,470 observations).

2.5 Air-sea CO_2 flux

To assess the global ocean carbon sink associated with our pCO_2 reconstructions, air-sea CO_2 exchange was calculated for 1985 onward. Here, we computed air-sea CO_2 fluxes using the bulk

Deleted:

Run name	5Y_J-A	10Y_J-A	10Y_YR
Saildrone track	One-lat	One-lat	One-lat
Years of sampling	5	10	10
# of Saildrones	1	1	1
Duration of sampling	Jan-Aug	Jan-Aug	Year-round
Total observations	2,075	4,150	4,150
Global coverage increase (%)	0.01	0.02	0.02

Deleted: Saildrone USV sampling patterns

Formatted: Font: 10 pt

Deleted: using the XGBoost Machine Learning algorithm (Gloege et al., 2021; Bennington et al., 2022a) to estimate surface ocean pCO_2

Deleted: The 'one-latitude' (

Deleted: o

Formatted: Font: 10 pt

Deleted:) track

Deleted: ,

Deleted: while the

Deleted: z

Deleted: track represents

Deleted: future

Deleted: (see **Fig. 2**)

Deleted: The total

Deleted: number of USV

Deleted: (in bold)

Deleted: represent

Formatted: Pattern: Clear

Formatted: Pattern: Clear

Formatted: Pattern: Clear

Formatted: Pattern: Clear

Formatted: Pattern: Clear

Formatted: Pattern: Clear

Deleted: Note that all runs also included SOCAT coverage.

formulation with python package Seaflux.1.3.1 (https://github.com/lukegre/SeaFlux; Gregor et al. 2021; Fay et al., 2021). We calculated global and Southern Ocean flux in the same manner for 1) the testbed ‘model truth’, 2) the ‘SOCAT baseline’ and 3) the 10 experimental USV runs.

Deleted:

The net sea–air CO_2 flux was estimated using:

$$Flux = k_w \cdot sol \cdot (pCO_2^{ocn} - pCO_2^{atm}) \cdot (1 - ice)$$

where ‘k_w’ is the gas transfer velocity, ‘sol’ is the solubility of CO_2 in seawater (in units of mol m^{-3} μatm^{-1}), ‘pCO_2^{ocn}’ is the partial pressure of surface ocean carbon (in µatm), either from the ‘model truth’ or from the reconstructions, and pCO_2^{atm} (in µatm) is the partial pressure of atmospheric CO_2 in the marine boundary layer. For GFDL, we used direct model output of pCO_2^{atm}, while for CESM and CanESM2, pCO_2^{atm} was calculated individually, as the product of surface xCO_2 and sea level pressure (the contribution of water vapor pressure was corrected for in CESM). Finally, to account for the seasonal ice cover in high latitudes, the fluxes were weighted by 1 minus the ice fraction (‘ice’), i.e., the open ocean fraction.

Deleted: pCO_2^{atm} from CESM was corrected for

Winds have the largest impact on flux calculations (Fay et al., 2021), and temporally high-resolution output is not available for the LET. Monthly output is available, but this is not sufficient for the flux calculation due to the square dependency of wind speed (Wanninkhof, 2014). Given the necessity to use observed winds, for consistency, we use observations for all necessary variables for the flux calculation. Inputs to the calculation include EN4.2.2 salinity (Good et al., 2013), SST and ice fraction from NOAA Optimum Interpolation Sea Surface Temperature V2 (OISSTv2) (Reynolds et al., 2002), and surface winds and associated wind scaling factor from the European Centre for Medium-Range Weather Forecasts (ECMWF ERA5 sea level pressure (Hersbach et al., 2020). Results presented show the global and Southern Ocean (< 35° S) fluxes in units of Pg C yr^{-1}.

Formatted: Highlight

Formatted: Indent: First line: 0.5"

Formatted: Highlight

Formatted: Highlight

Formatted: Font color: Auto

Note that, reconstructions of pCO_2 for the ‘SOCAT baseline’ and the experimental USV runs are limited in their spatial extent to the open ocean (see **Sect. 2.1**; excluding coastal areas, the Arctic Ocean and marginal seas). The same mask was thus also applied when calculating the flux of the ‘model truth’, prior to comparison with the reconstructions.

Deleted:

3. Results

3.1 Performance metrics for the 'SOCAT-baseline' reconstruction

The mean bias for the entire testbed period (i.e., 1982-2016) is 0.63 µatm globally (**Fig. 3a**) and 1.4 µatm for the Southern Ocean (< 35° S; **Table 1**). Bias is much closer to zero for the mid-latitudes (between 35° S and 35° N; 0.23 µatm) and northern latitudes (> 35° N; 0.11 µatm) (**Fig. 3a**). There is a significant difference in bias considering southern hemisphere winter months (June, July, August) versus summer months (December, January, February), with a global mean bias (for 1982-2016) of 1.3 µatm compared to 0.07 µatm, respectively (**Table 1**), due to the sparseness of SOCAT observations from the southern hemisphere during the harsh winter season (**Fig. S5a**). The mean RMSE for the entire testbed period (i.e., 1982-2016) is 11.8 µatm globally (**Fig. 3b**) and 11.5 µatm for the Southern Ocean (**Table 1**). RMSE is highest in the Eastern Tropical and Southeastern Pacific Ocean and in the Southern Ocean, where the algorithm generally overestimates pCO_2 (i.e., positive bias; **Fig. 3a**), with some exceptions in the Atlantic section. This is consistent with the areas significantly undersampled by SOCAT (**Fig. S5b**). Except for these areas, RMSE and bias is generally low (close to zero) in the open ocean, but show higher values along coastlines (**Fig. 3b**). The predicted pCO_2 is thus more accurate in areas similar to and surrounding the SOCAT "observations" (i.e., monthly 1°x1° grid cells equivalent to SOCAT coverage, but sampled from the LET). **Figure 3** shows mean bias and RMSE for the full reconstruction (see **Section 2.3**), but note that there is a statistically significant difference between the train and test set errors (**Fig. S6**). This indicates potential overfitting in our ML model (i.e., higher errors for the 'unseen' reconstruction), and that further tuning of the hyperparameters could increase generalization skill (see **Supplementary Text A**).

Deleted:
Deleted: S
Deleted: S
Deleted: 3
Deleted: 7
Deleted: 9
Deleted: 8
Deleted: S
Deleted: 3
Formatted: Subscript
Formatted: Highlight
Formatted: Font: 12 pt, Not Italic, Highlight
Formatted: Highlight
Formatted: Highlight
Formatted: Font: Bold, Highlight
Formatted: Highlight
Formatted: Highlight
Formatted: Font: Bold, Highlight
Formatted: Highlight
Formatted: Highlight
Formatted: Font: Bold, Highlight
Formatted: Highlight
Formatted: Highlight
Formatted: Font: Bold, Highlight
Formatted: Font: Bold

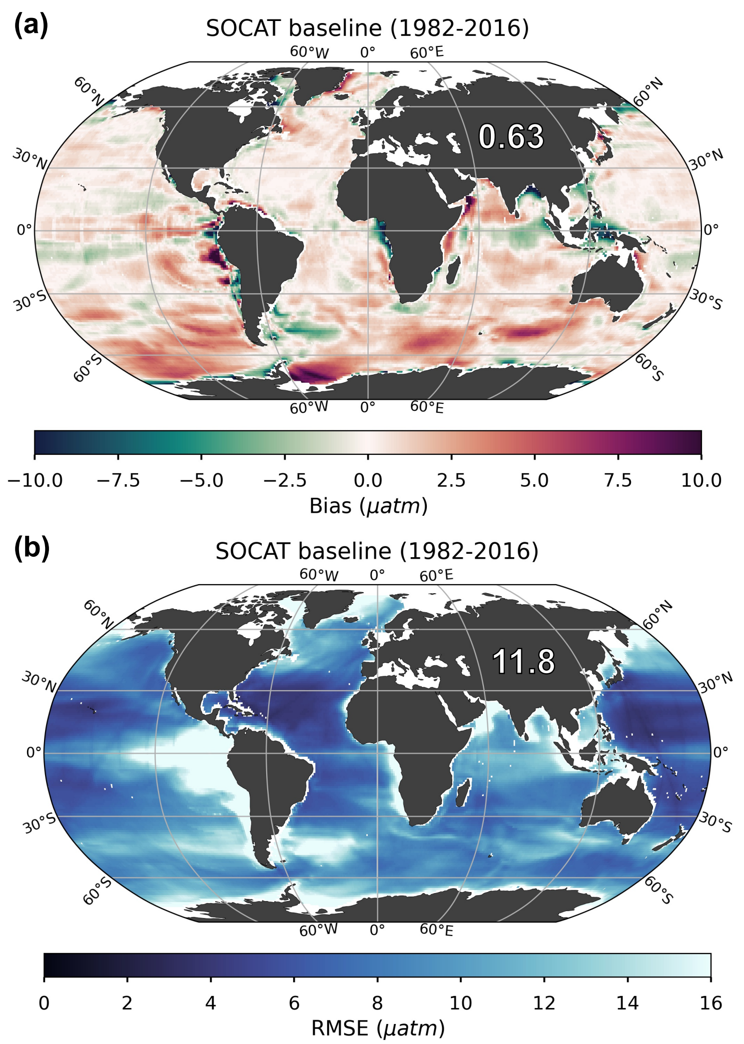

Figure 3: Bias (**a**) and root-mean-squared error (RMSE) (**b**) for the 'SOCAT-baseline' (i.e., no USV) over the period of 1982 through 2016. The global mean bias and RMSE is 0.63 μatm and 11.8 μatm, respectively. Note that only the open ocean was considered in the reconstruction, so several areas were masked out prior to algorithm processing, such as the Arctic Ocean, coastal areas and marginal seas (no data; white areas in figures).

3.2 Reconstruction improvements with Saildrone USV additions

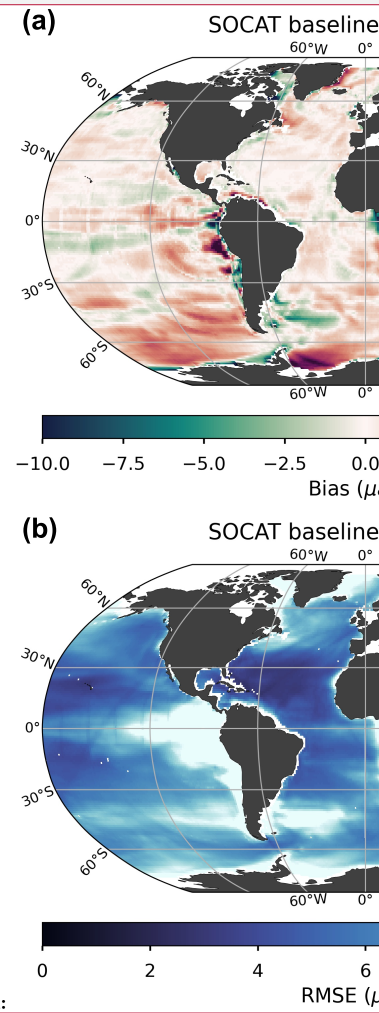

Deleted:

Deleted: B

Deleted: when comparing the baseline machine learning reconstruction with the testbed 'model truth', averaged over the 75 ensemble members for the period of 1982 through 2016. The testbed was sampled based on SOCAT observations only (i.e., no USV).

Deleted: 7

Deleted: 9

Deleted: Red and green areas in **a** indicate regions where the reconstruction is biased high (i.e., overestimates pCO_2) and low (i.e., underestimates pCO_2), respectively. Generally, RMSE is highest in the East and South Pacific Ocean and in the Southern Ocean, where the algorithm also generally overestimates pCO_2 (positive bias; **a**).

Our presentation of global maps is limited to runs 'x5_5Y_W' (5,022 monthly 1°x1° observations) and 'Z_x4_10Y_YR' (7,600 monthly 1°x1° observations). These runs were selected as they represent observational schemes that are realistic in the near-term future considering logistics and cost level, both non-meridional and meridional sampling, and different approaches to observing duration and seasonal coverage. For the remaining runs, equivalent maps can be found in the **Supplement**.

3.2.1 Bias

All Saildrone USV runs show a reduction in bias compared to the global mean 1982-2016 'SOCAT-baseline' (**Figs. 4a**, **S7**). The improvement in bias is mainly due to lower reconstructed pCO_2 values at southern latitudes, where the 'SOCAT-baseline' reconstruction generally overestimates pCO_2 (**Fig. 3a**). The global mean bias for 'zigzag' run 'Z_x4_10Y_YR' is 0.51 µatm, a higher improvement (19 %) over the 'SOCAT-baseline' compared to the 'one-latitude' run 'x5_5Y_W' (11 % mean improvement; mean bias = 0.57 µatm;) (**Fig. 4a**; **Table 1**). Generally, the 'zigzag' runs show higher improvements from the 'SOCAT-baseline' (19-31 % improvement; resulting mean bias = 0.44-0.51 µatm) compared to the 'one-latitude' runs (7-19 % improvement; resulting mean bias = 0.52-0.59 µatm) (**Fig. S6**; **Table 1**). However, the 'one-latitude'-run 'x13_10Y_W' that samples southern hemisphere winter months only, stands out with the lowest global mean (1982-2016) bias of 0.39 µatm, representing a 39 % mean improvement from the 'SOCAT-baseline' (**Table 1**; **Fig. S7**). This run, however, has three and five times more observations (25,395) than 'Z_x4_10Y_YR' and 'x5_5Y_W', respectively.

Compared to the entire testbed period, even larger improvements in global mean bias are shown for the period of Saildrone USV additions (2006-2016 and 2012-2016; **Figs. 4a** vs. **4b**, **Figs. S7** vs. **S8**). Compared to the 'SOCAT-baseline', run 'x13_10Y_W' results in a mean bias improvement of 95 %, while the remaining 'one-latitude' runs and the 'zigzag' runs show mean improvements up to 63 % and 85 %, respectively (**Fig. S8**). The spread in mean bias (2006/2012-2016) across the 75 testbed members for each experiment is shown in **Figure S9.**

Perhaps surprisingly, there is not a strong connection between the global or Southern Ocean mean bias and the number of added USV observations (**Fig. 5**). The 'one-latitude' 'high-sampling' run 'x13_10Y_J-A' (44,250 observations) show similar mean bias or is outperformed by all

Deleted:
Deleted: 4
Deleted:
Deleted: S
Deleted:
Deleted: 4
Deleted: S
Deleted:
Deleted: S
Deleted: 4
Deleted: or
Deleted: 4
Deleted: 5
Deleted:
Deleted: 5

'zigzag' runs as well as the 'one-latitude'-runs that restrict sampling to southern hemisphere winter months (i.e., 'x5_5Y_W' and 'x13_10Y_W').

Considering the change in bias from year-to-year, the 'SOCAT-baseline' shows positive bias at all latitudes in the beginning of the testbed period, before improvement occurs around 1990 (**Fig. 6a**). This is consistent with increasing SOCAT sampling with time for the period considered here (i.e., up to 2016; **Fig. S5c**). As SOCAT observations are biased towards the northern hemisphere (**Fig. S5a, b**), bias in the Southern Ocean (< 35° S) increases significantly starting in the 2000s and remains high until the end of the testbed period (**Fig. 6a**). By adding USV sampling, bias in the Southern Ocean improves over the 'SOCAT-baseline' around year 2000 (**Fig. 6b-d**; **Fig. S10**), up to 6-12 years before to the introduction of additional samples in either 2006 or 2012. This improvement is shown for the majority of the 75 ensemble members (**Fig. S11**). Run 'Z_x10_5Y_W', which has the lowest mean bias out of the 'zigzag' runs (**Fig. 5**), shows improvement even further back in time, until the beginning of the testbed period (**Fig. S10**). While the annual mean bias of the 'zigzag' runs varies rather consistently, there is a larger spread across the 'one-latitude' runs (**Fig. 6d**).

Deleted:

Deleted: year

Deleted: time

Deleted: 3

Deleted: 3

Deleted:

Deleted: 6

Deleted: prior

Formatted: Font: Bold

Deleted: 6

Deleted: vary

Deleted: in a similar manner

Deleted: between

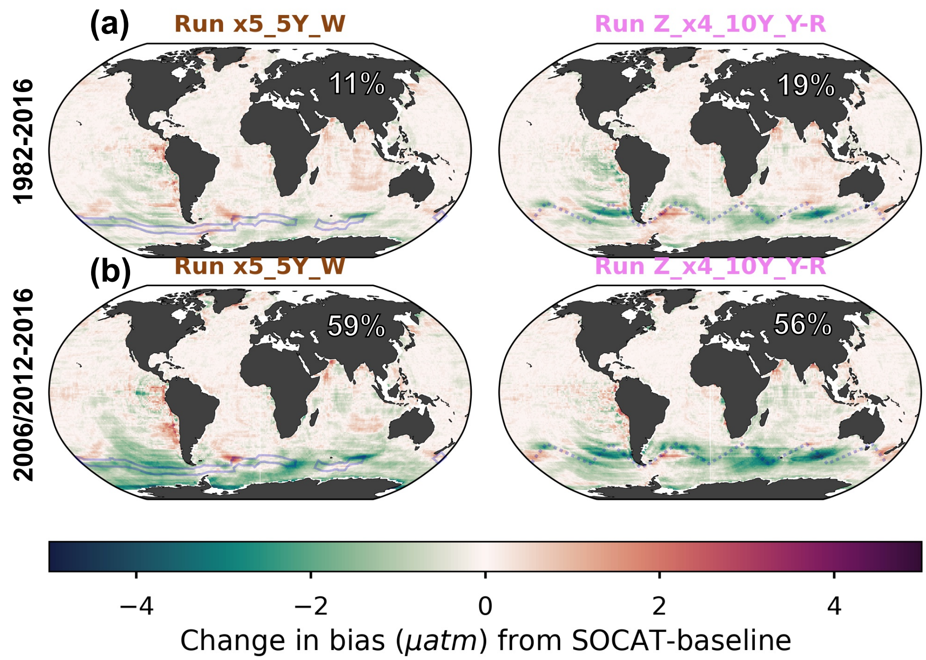

Figure 4: Change in bias when comparing run 'x5_5Y_W' and 'Z_x4_10Y_YR' to the 'SOCAT-baseline' reconstruction, averaged over the duration of the testbed period (**a**; 1982-2016) and the period of USV additions (**b**; 2006-2012 or 2012-2016). The percent global improvement in absolute bias is shown on each panel. The USV Saildrone tracks are shown in blue.

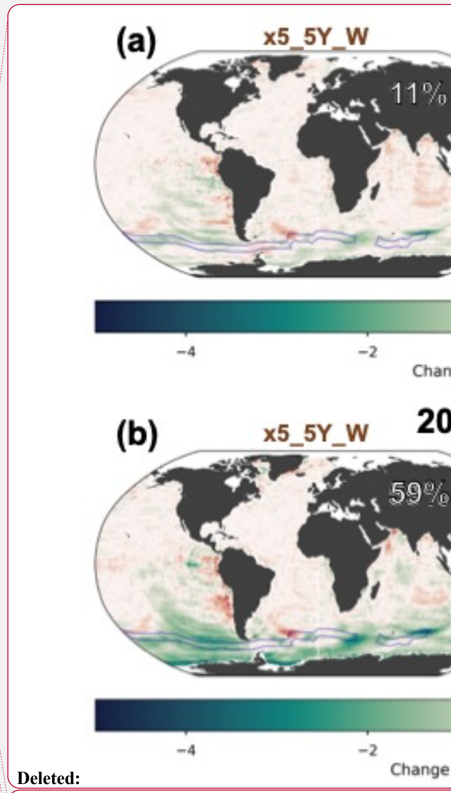

Deleted:

Deleted:

Deleted: Negative change in bias is found across the southern latitudes, indicating an improvement compared to the SOCAT baseline that overestimates pCO_2 (**Figure 3a**).

Formatted: Highlight

Deleted: Note that improvement is greater in the period of Saildrone USV additions compared to the entire testbed period. ...

Formatted: Highlight

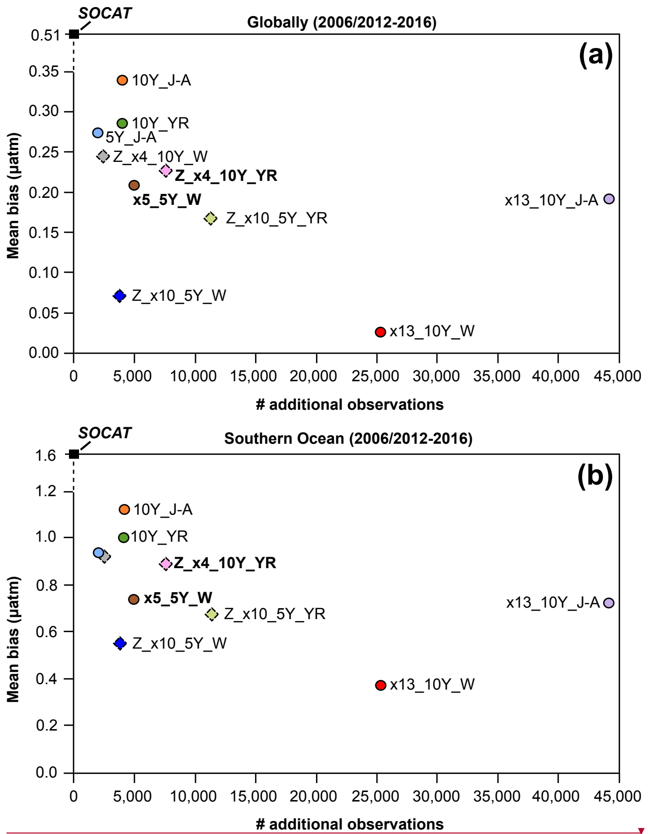

Figure 5: Mean bias globally (**a**) and for the Southern Ocean (**b**) for the duration of Saildrone USV sampling (2006-2016 or 2012-2016) for all runs presented in **Table 1**. Circles represent runs using the 'one-latitude' track, while diamonds represent 'zigzag' runs. Runs highlighted in bold correspond to the two selected runs mapped in **Figure 4, 6, 7** and **9**. Global (0.51 µatm) and Southern Ocean (1.6 µatm) bias values shown for the 'SOCAT baseline' (black squares) represent a mean of values for 2006-2016 (global = 0.52 µatm, S. Ocean = 1.63 µatm) and 2012-2016 (global = 0.51 µatm, S. Ocean = 1.56 µatm). '# additional observations' = number of monthly 1°x1° USV observations in addition to SOCAT. Box plots illustrating the spread across the 75 ensemble members are shown in **Fig. S9**.

Deleted:

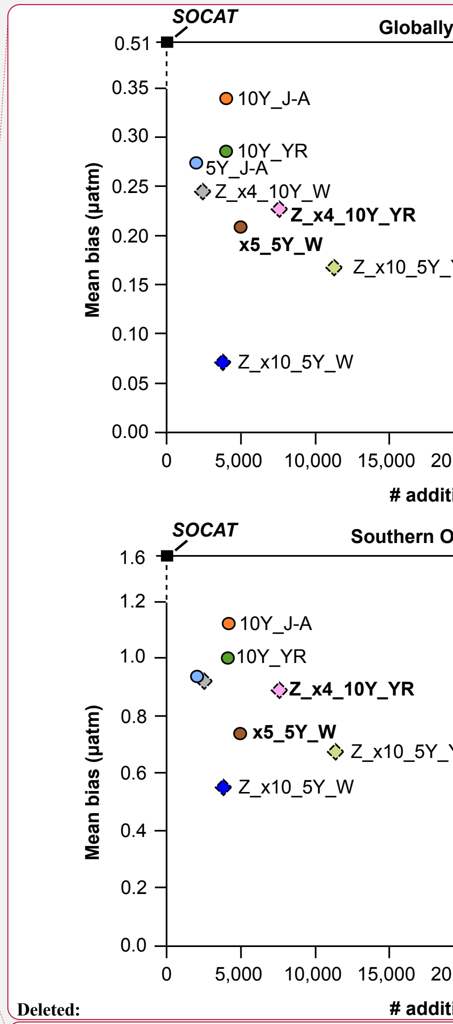

Deleted: (Sutton et al., 2021)

Deleted:

Deleted: The SOCAT baseline run included 261,733 monthly 1°x1° observations.

Formatted: Font: Bold

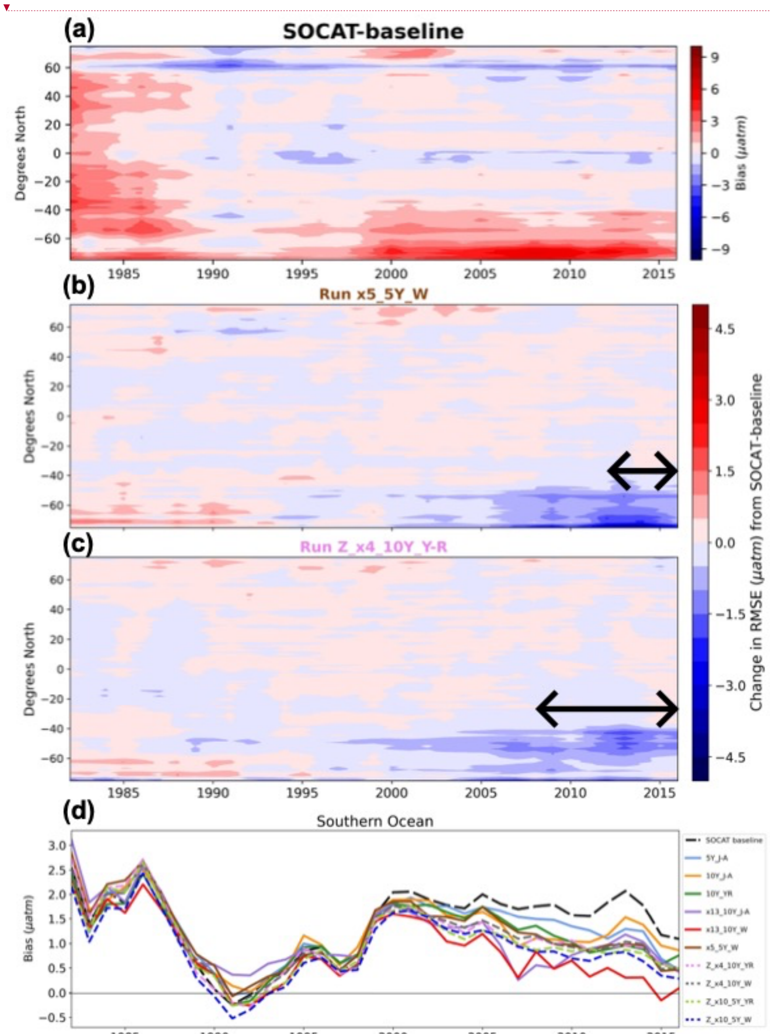

Figure 6: Zonal mean, annual mean Hovmöller of bias for the 'SOCAT baseline' (**a**). Change in bias for run 'x5_5Y_W' (**b**) and 'Z_x4_10Y_YR' (**c**) compared to the 'SOCAT baseline' shown in (**a**). Improvement in bias in the Southern Ocean expands back in time well beyond the duration of USV additions for both runs (shown by arrows on each panel). Annual mean bias for the Southern Ocean (> 35° S) for all runs (**d**).

Deleted: Overall, there is not a strong correlation between bias and the number of observations, or duration of sampling.

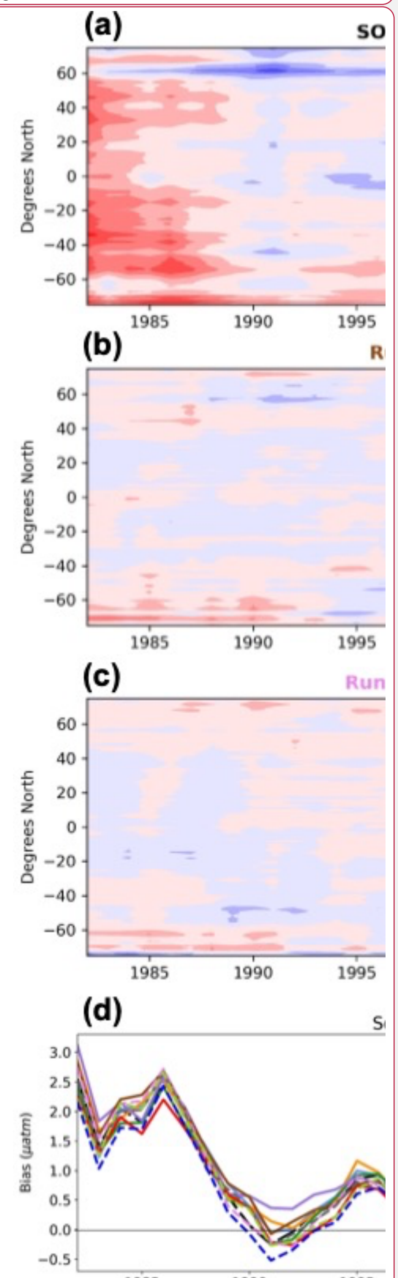

Deleted: ... [1]

3.2.2 Root-mean squared error (RMSE)

Similar to bias, improvements in RMSE are most significant during the period of USV additions and within the Southern Ocean (**Fig. 7a** vs. **7b**). For the duration of USV additions, the 'one-latitude' runs show improvements in global mean RMSE of 1-3 % (0.1-1 % for 1982-2016), while the 'zigzag' runs show higher improvements between 2-5 % (1-3 % for 1982-2016) (**Figs. 7**, **S12**, **S13**). Mean RMSE is further reduced in the Southern Ocean by up to 16 %, and during southern hemisphere winter months (JJA) up to 21 % (run 'Z_x10_5Y_YR'; mean RMSE of 9.6 µatm; **Table 1**). There is minimal change in RMSE (or bias) during southern hemisphere summer months (DJF; **Fig. S14**). The two 'zigzag' runs sampling year-round ('Z_x4_10Y_YR' and 'Z_x10_5Y_YR') have the lowest RMSE values both globally and in the Southern Ocean (**Fig. 8**). The spread across the 75 testbed members for each experiment is shown in **Figure S15**.

The 'zigzag' runs, as well as the 'high-sampling' 'one-latitude'-runs (i.e., 'x13_10Y_J-A' and 'x13_10Y_W'), show improvements compared to the 'SOCAT-baseline' from the initiation of sampling (**Figs. 9**, **S16**, **S17**). The year-round 'zigzag' runs, however, show improvement in the Southern Ocean from the beginning of the testbed period (**Figs. 9c**, **d**, **S16**). RMSE improvements back in time are greater for all runs in the southern hemisphere winter months (**Fig. S18**).

Deleted: 4
Deleted: 3
Deleted: 2
Deleted: 3
Deleted: 8
Deleted: 2
Deleted: 7
Deleted: **8**
Deleted: in the Southern Ocean by
Deleted: 6
Deleted: 6
Deleted: 9
Deleted: **S**
Deleted: **9**
Deleted: '
Formatted: Font: Bold
Deleted:
Deleted: **0**
Formatted: Font: Not Bold
Deleted: **0**
Deleted: more significant
Deleted: **1**

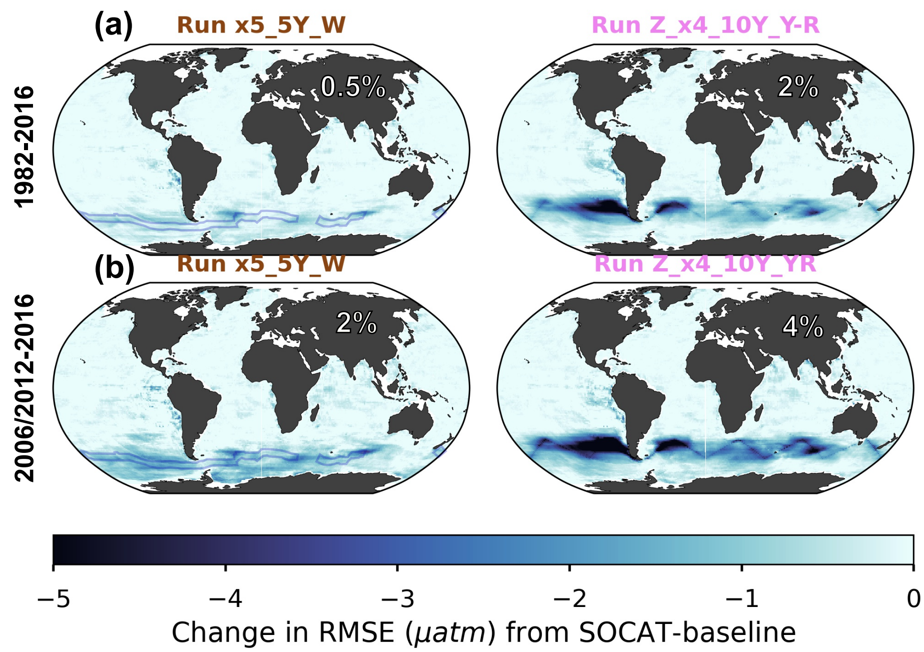

Figure 7: Change in RMSE when comparing run 'x5_5Y_W' and 'Z_x4_10Y_YR' to the 'SOCAT baseline' averaged over the duration of the testbed period (**a**; 1982-2016) and the period of Saildrone USV additions (**b**; 2006-2012 or 2012-2016). The percent global improvement is shown on each panel.

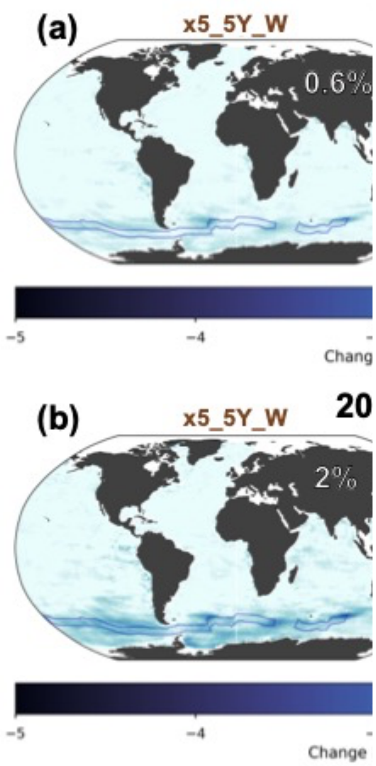

Deleted:

Deleted:

Deleted: reconstruction

Deleted: Improvement in RMSE occurs mainly in southern latitudes (<35°S), where the baseline reconstruction shows high RMSEs (**Fig. 3b**).

Deleted: Note the greater improvement for the period of USV additions compared to the entire testbed period.

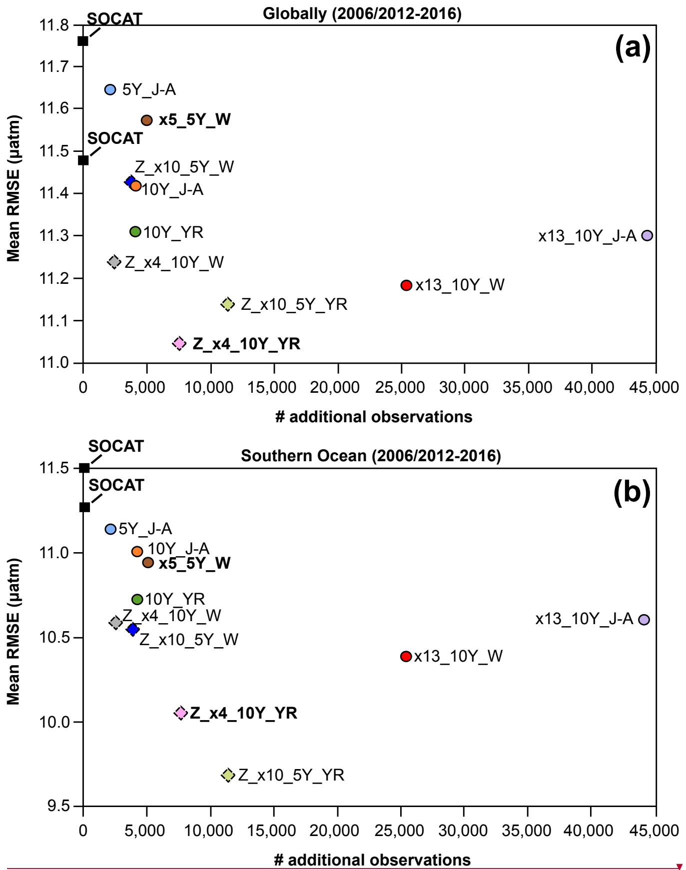

Fig. 8: Mean RMSE globally (**a**) and for the Southern Ocean (< 35° S; **b**) for the duration of Saildrone USV sampling (2006-2016 or 2012-2016) for all runs presented in **Table 1**. Circles represent runs using the 'one-latitude' track, while diamonds represent 'zigzag' runs. Runs highlighted in bold correspond to the two selected runs mapped in **Figure 4, 6, 7** and **9**. RMSE values shown for the 'SOCAT-baseline' (black squares) represent a mean of values for 2006-2016 (global = 11.5 µatm, S. Ocean = 11.3 µatm) and 2012-2016 (global = 11.8 µatm, S. Ocean = 11.5 µatm). '# additional observations' = number of monthly 1°x1° USV observations in addition to SOCAT. Box plots illustrating the spread across the 75 ensemble members are shown in **Fig. S15**.

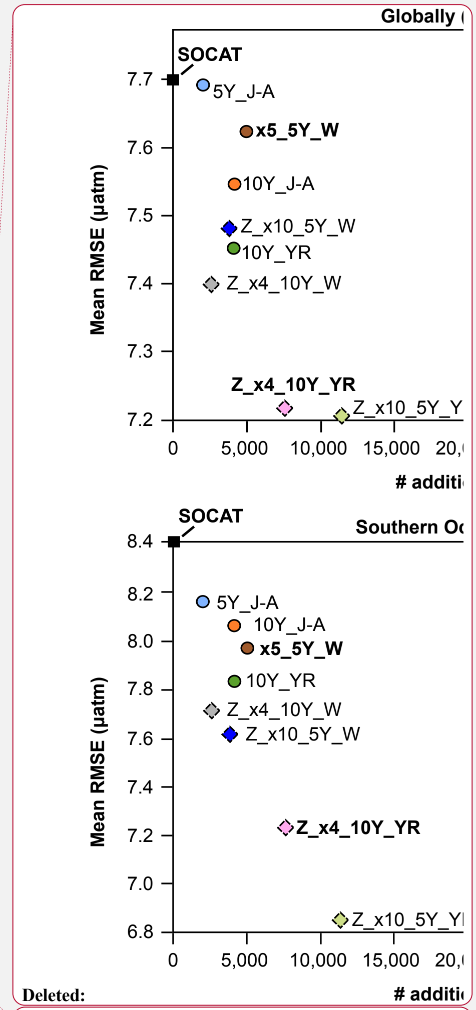

Deleted:

Deleted: 'One-latitude' runs (circles), 'zigzag' runs (diamonds). …

Deleted: Global (7.7 µatm) and Southern Ocean (8.4 µatm)

Deleted: bias

Deleted:

Deleted: 7.6

Deleted: 8

Deleted: 7

Deleted: 8

Deleted: The SOCAT baseline run included 261,733 monthly 1°x1° observations.

Deleted: Overall, there is not a strong correlation between increasing number of observations or duration of sampling and decreasing RMSE.

Formatted: Font: Not Italic

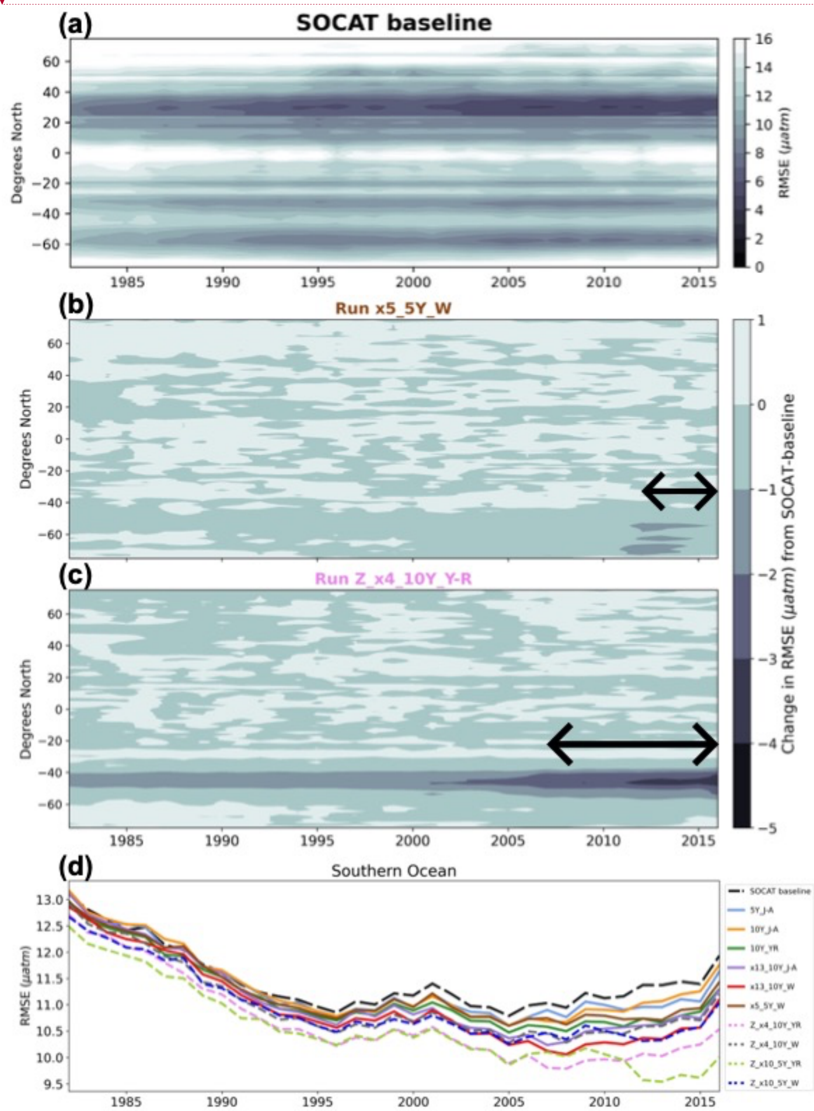

Figure 9: Zonal mean, annual mean Hovmöller of RMSE for the 'SOCAT-baseline' (**a**). Change in RMSE for run 'x5_5Y_W' (**b**) and 'Z_x4_10Y_YR'(**c**) compared to the 'SOCAT-baseline'. Run 'Z_x4_10Y_YR' shows improvement in RMSE within the Southern Ocean, which expand well beyond the duration of Saildrone USV additions (shown by arrow on panel). Annual mean RMSE for the Southern Ocean (> 35° S) for all runs (**d**).

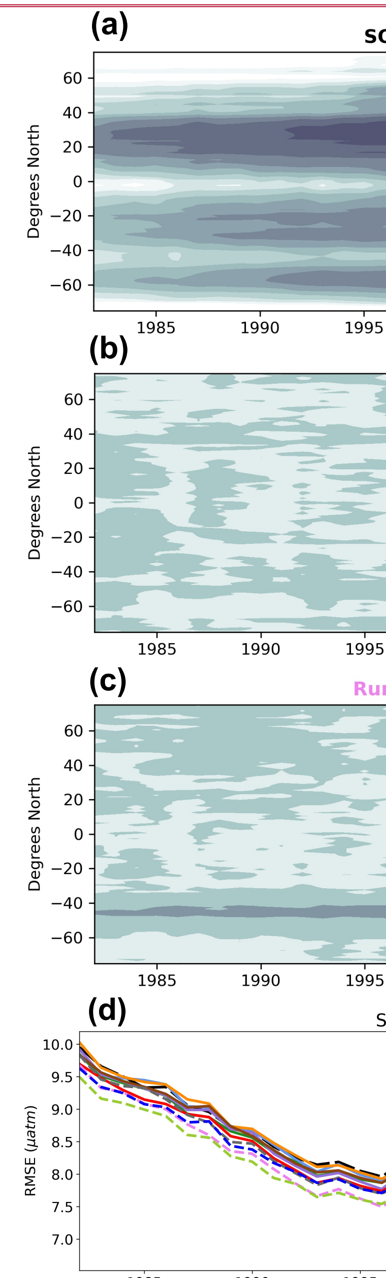

Deleted:

Deleted: in…'SOCAT- …aseline' (with the testbed 'model truth', average of 75 ensemble members (…). Dark and light areas represent regions where RMSE is low and high, respectively. RMSE is highest at latitudes > 60° S, > 60° N and around 40° S and the equator. RMSE is higher at all latitudes in the beginning of the testbed period, before some improvement occurs in the 1990s. …hange in RMSE forof…run 'x5_5Y_W' (**b**) and 'Z_x4_10Y_YR'(**c**) compared to the 'SOCAT- …aseline' reconstruction shown in (**a**)… Dark areas represent regions where the change in RMSE is negative, i.e., where the Saildrone USV samp ... [2]

Formatted: Line spacing: single

3.3 Impact on the air-sea CO_2 flux with Saildrone USV additions

Air-sea flux was calculated in the same manner for both the ML reconstructions and the 'model truth', which allows for the isolation of the impact of different sampling strategies, as mediated by the pCO_2 reconstruction, on fluxes (see **Sect. 2.5**). These flux estimates are made to inform understanding of the errors that may exist in CO_2 flux estimates derived from pCO_2 reconstructions, and how new sampling could address these errors. Flux estimates represent the average of the 75 members of the LET in each case, and are not estimates of real-world fluxes.

Compared to the 'model truth', the 'SOCAT-baseline' reconstruction underestimates the global and Southern Ocean sink by 0.11-0.13 Pg C yr^{-1} over 1982-2016 (**Fig. 10**; **Table S1**). Regardless of sampling pattern, adding Saildrone USV observations increases both the global and Southern Ocean mean sink compared to the 'SOCAT-baseline' (**Figs. 10**, **S19**). The 'one-latitude' runs show an increase of 0.01-0.03 Pg C yr^{-1} (2-6 % strengthening) of the Southern Ocean sink (1982-2016), while the 'zigzag' runs lead to an even stronger sink by 0.04-0.06 Pg C yr^{-1} (7-11 % strengthening) (**Table S2**). When averaging over the years of Saildrone USV sampling addition (i.e., 2006-2012 and 2012-2016), the Southern Ocean sink increases up to 0.09 Pg C yr^{-1} (14 % strengthening) for the 'one-latitude' runs and up to 0.1 Pg C yr^{-1} (15 % strengthening) for the 'zigzag' runs (**Table S2**). These same features are found for the global ocean (**Fig. S19**; **Table S2**).

All of the 'zigzag' runs quite closely match both the global and Southern Ocean 'model truth' air-sea CO_2 flux for the duration of sample additions (**Figs. 10**, **S19**). Except for the first couple of years of sample addition for the 'high-sampling'-run 'x13_10Y_J-A', none of the 'one-latitude' runs can match the 'model truth' air-sea CO_2 flux, instead they all underestimate the flux (**Figs. 10, S19**). The 'zigzag' runs have impact on the air-sea flux from an earlier date, starting to pull the results away from the 'SOCAT-baseline' and toward the 'model truth' already in the late-1990s, while the 'one-latitude' runs do the same about a decade later (**Figs. 10**, **S19**).

Deleted: direct comparison of the differences in

Formatted: Subscript

Deleted: These fluxes

Deleted:

Deleted: 2

Deleted:

Deleted: 2

Deleted: 3

Deleted: 3

Deleted: 2

Deleted: 3

Deleted: 2

Deleted: are able to

Deleted: as

Deleted: 2

Deleted:

Deleted: 2

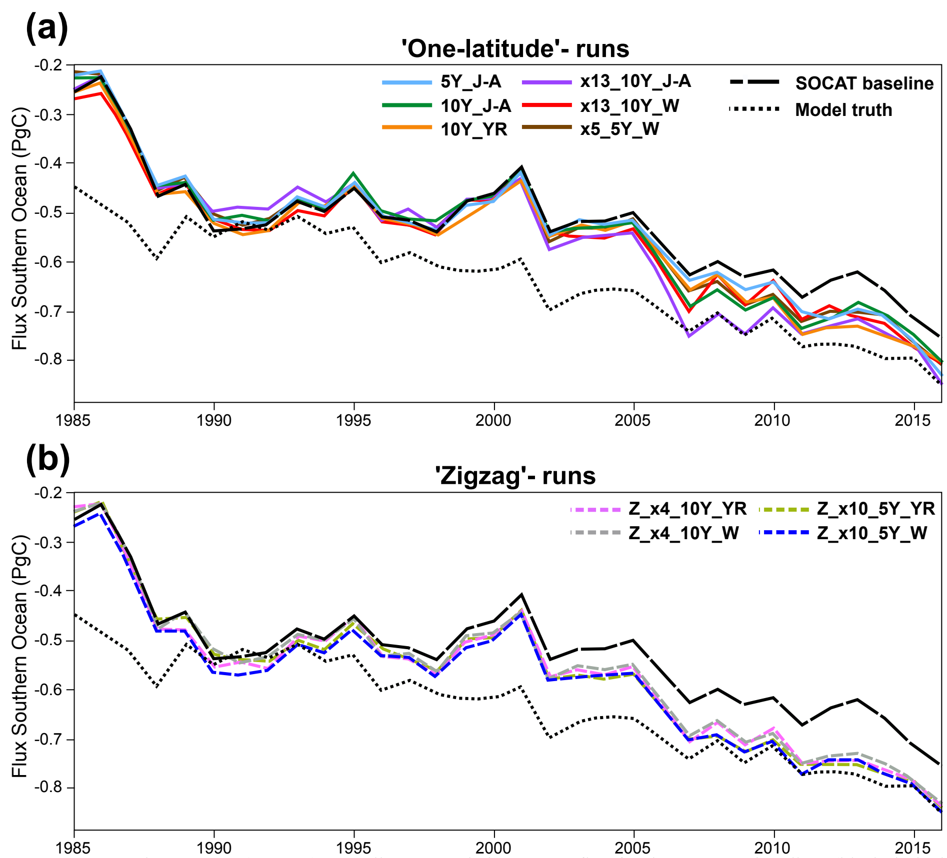

Figure 10: Southern Ocean (< 35° S) annually averaged air-sea CO_2 flux for the 'SOCAT baseline' (black dashed line), 'model truth' (black dotted line) 'one-latitude' runs (**a**; solid lines) and 'zigzag' runs (**b**; dashed lines).

Deleted:

Deleted: , averaged over the 75 ensemble members

Deleted: Compared to the SOCAT baseline, regardless of sampling pattern, the Saildrone USV additions lead to an increased ocean sink. The 'zigzag' runs generate a stronger sink compared to the 'one-latiude' runs, and closely match the 'model truth' for the duration of sample additions.

4. Discussion

We have tested the pCO_2-Residual reconstruction method with the Large Ensemble Testbed (LET) to estimate its fidelity and understand how new samples could increase skill. We find that, regardless of the chosen Saildrone USV sampling pattern, the reduction in mean bias and mean RMSE compared to the 'SOCAT baseline' is most prominent within the Southern Ocean (< 35° S) during the period of which Saildrone USV observations were added (**Figs. 4, 6, 7, 9**). However, it is important to mention that the additional Southern Ocean sampling also impacts (improves)

Deleted: both

Deleted:

the pCO_2 reconstructions globally (**Figs. 5a**, **8a**). Based on our experiments, a combination of factors improve global and Southern Ocean pCO_2 reconstructions, including the type of sampling pattern and seasonality of sampling, and to some extent, the number of additional observations. Importantly, increasing the number of observations or duration of sampling (5 vs. 10 years) is not the sole determining factor for improving the reconstructions (**Figs. 5**, **8**). This is best demonstrated by the 'high-sampling'-run 'x13_10Y_J-A' (44,250 observations), which does not provide significantly better reconstructions, or is even outperformed, by runs with 2-18 times fewer observations. The runs that produce lower mean RMSE do include data throughout southern hemisphere winter (**Fig. 8**). Run 'x13_10Y_J-A' does not include more than a few observations in the month of August, as it follows the temporal pattern of the real-world 'one-latitude' Saildrone USV expedition (**Figs. S3, S4**; Sutton et al., 2021). The 'one-latitude' runs '10Y_J-A' and '10Y_YR' are directly comparable in terms of sample duration, spatial extent and number of observations (**Table 1**), but the latter, which covers all months, always shows lower mean RMSE and bias (**Figs. 5**, **6d**, **8**, **9d**). These examples attest to the importance of addressing the issue of significant undersampling in the Southern Ocean during the winter season (**Fig. S5a**).

Another important comparison is the 'one-latitude'-run 'x5_5Y_W' (5,022 observations) and 'zigzag'-run 'Z_x10_5Y_W' (3,800 observations) that both sample during southern hemisphere winter months over a five-year period (**Table 1**), where the 'zigzag'-run consistently performs better even though it includes fewer observations (**Figs. 5**, **8**). Most of the runs that perform similar to, or outperform, the above-mentioned 'high-sampling'-run 'x13_10Y_J-A' (44,250 observations), sample in a 'zigzag' pattern. Out of all 10 runs, the 'year-round' 'zigzag' runs ('Z_x4_10Y_YR' and 'Z_x10_5Y_YR') are most able to reduce the mean error as shown by the lowest RMSE values (**Figs. 8**, **9d**). A recent study performed similar sampling experiments as shown here, by comparing sampling from different types of autonomous platforms to a 'SOCAT-baseline' (Djeutchouang et al., 2022). They emphasized the importance of capturing the significant differences in pCO_2 that exist across meridional gradients during summer and winter months (up to 15 µatm; Djeutchouang et al., 2022). The meridional coverage provided by the 'zigzag' runs could explain why these runs generally outperform the 'one-latitude' runs in our study, and show significant reduction in both RMSE and bias, even though the global pCO_2 data density is raised by as little as 0.01-0.07 %.

Deleted: seems to be important in order to

Deleted: both the

Deleted: and

Deleted: e

Deleted: mainly

Deleted: but also

Deleted: 2-18 times less

Deleted: , but that cover the full

Deleted: s

Deleted: 5, **6d**,

Deleted: , **9d**

Deleted: 1

Deleted: s

Deleted: 3

Deleted: , b

Deleted: magnitude of

Deleted:

Deleted: 4

The greatest reduction in mean bias out of all runs is shown by run 'x13_10Y_W' (**Figs. 5**, **6d**), which represents 'one-latitude' 'high-sampling' (i.e., 25,395 observations) during southern hemisphere winter months only. This sampling strategy seems thus to have a higher ability to reduce the ML model's tendency to overestimate pCO_2 in the Southern Ocean compared to any of the meridional ('zigzag') runs. However, it should be noted that run 'x13_10Y_W' covers areas south of 55° S (**Fig. S4**), and its improvement in mean bias (and mean RMSE) is particularly prevalent at these high latitudes (e.g., **Figs. S8**, **S10**, **S13**, **S16**). Whether or not this run is, in fact, feasible with current or future technology is uncertain as parts of the southernmost tracks potentially cover the Southern Ocean ice zone (**Fig. S20**), and solar radiation for solar-powered platforms and sensors becomes very limited during winter south of 55° S. Furthermore, this particular sampling strategy requires 13 USVs, and so would be the most costly of the observing scenarios. Although run 'x13_10Y_W' demonstrates the highest reduction in mean bias out of all runs, the 'zigzag' runs still reduce absolute mean bias (for 2006/2012-2016) in the Southern Ocean by 44-65 % (vs. 77 % for run 'x13_10Y_W').

Overall, the 'zigzag' runs include significantly fewer observations, require fewer USVs, collect samples over the same duration, or even half the time as run 'x13_10Y_W', cover areas north of 55°S and within the ice-free zone, and show major improvement in the reconstruction of pCO_2, attested to by reductions in both bias and RMSE. The 'zigzag' runs also closely match both the global and Southern Ocean 'model truth' air-sea CO_2 flux for the duration of sample additions (**Figs. 10**, **S19**). It also appears that the 'zigzag' runs generally have a greater impact on both the pCO_2 reconstruction and the air-sea flux further back in time, starting to deviate from the 'SOCAT-baseline' earlier compared to the 'one-latitude' runs (**Figs. 6**, **9**, **10**, **S10**, **S16**, **S18**, **S19**). Even the 'zigzag' scenarios with the least number of USVs (e.g., 'Z_x4_10Y_YR') reduces Southern Ocean reconstruction absolute mean (2006-2016) bias and RMSE by up to 46 % and 11 %, respectively, and could provide a basis for realistic future Southern Ocean pCO_2 sampling campaigns.

The main motivation for improving surface ocean pCO_2 reconstructions is so that we can more accurately estimate the current and future oceanic uptake of anthropogenic carbon. The Southern Ocean is a significant carbon sink, but estimates of the air-sea CO_2 flux diverge substantially in this region (Takahashi et al., 2009; Landschützer et al., 2014, 2015; Rödenbeck et al., 2015; Williams et al., 2017; Gray et al., 2018; Gruber et al., 2019; Bushinsky et al., 2019; Long

Deleted: i
Deleted: however
Deleted: 2
Deleted: such
Deleted: 5
Deleted: 6
Deleted: 8
Deleted: 0
Deleted: 13
Deleted: thus
Deleted: less
Deleted: 2
Deleted:
Deleted: 6
Deleted: 0
Deleted: 1
Deleted: 2
Deleted: 3

et al., 2021; Fay and McKinley, 2021; Wu et al., 2022). Southern Ocean estimates incorporating observations from biogeochemical floats have shown a significantly weaker sink compared to those based only on observations from ships (Williams et al., 2017; Gray et al., 2018; Bushinsky et al., 2019). Bushinsky et al. (2019) and Hauck et al. (2023) performed similar sampling experiments as presented here, by comparing ML surface ocean pCO_2 reconstructions based on SOCAT vs. additional SOCCOM or ideal virtual floats. These studies showed that SOCAT sampling alone overestimates the CO_2 uptake in the Southern Ocean, and that additional floats reduce this overestimation, leading to a decreased (weakened) ocean carbon sink. In contrast, we find that the pCO_2-Residual method underestimates the CO_2 uptake with only SOCAT sampling, and that adding USVs increased (strengthened) the Southern Ocean and global ocean sink by up to 0.1 Pg C yr^{-1} (**Figs. 10**, **S19**; **Table S2**).

Going forward, additional studies are needed to better understand why these results suggest a different direction of the sink change with additional sampling. These differences could stem from the use of different reconstruction methods assessed. Hauck et al. (2023) used the MPI-SOM-FFN and CarboScope/Jena-MLS reconstruction methods, while we use the pCO_2-Residual method. Another substantial difference between the studies is the models and numbers of ensemble members used as the testbed. Hauck et al. (2023) use a single hindcast model, while we use 25 members each from three Earth System Models. We find substantial spread across these 75 members (**Figs. S9 S15**), indicating that model structure and internal variability significantly impact results. Our study and Hauck et al. (2023) use different sampling masks and approaches for the calculation of fluxes, which could also be a factor. Targeted, coordinated studies using multiple reconstruction approaches with consistent testbed structures, sampling masks and experimental approaches are clearly needed (Rödenbeck et al., 2015). Despite this need for this additional work, studies do agree that additional Southern Ocean observations could significantly improve reconstructions of air-sea CO_2 fluxes.

What else can we learn using the model testbed? The 'SOCAT-baseline' demonstrates a weakening of the global and Southern Ocean carbon sink starting in the 1990s with a peak around year 2000 (**Figs. 10**, **S19**), which is in broad agreement with various data products using real-world SOCAT data (e.g., Gruber et al., 2019; Landschützer et al., 2015; Bushinsky et al., 2019; Bennington et al., 2022; Gloege et al., 2022). Peaks in bias and RMSE coincide in time with the

Deleted: alone
Deleted: Southern Ocean
Deleted: They
Deleted: by
Deleted: ng
Deleted: the
Formatted: Subscript
Deleted: , the Southern Ocean carbon sink (mean of the period of float additions; 2015-2017) decreased (weakened) by 0.4 Pg C yr^{-1}. In contrast,
Deleted: by using a model testbed, we show that
Formatted: Subscript
Formatted: Subscript
Deleted: 2
Deleted: 3), which is a significant fraction of the uncertainty in the global ocean carbon sink (0.4 Pg C yr^{-1}; Friedlingstein et al., 2022
Deleted: Fed with real-world SOCAT data, the global mean air-sea flux estimate from the pCO_2-Residual method is similar to other available products (Bennington et al., 2022a), suggesting that other products may also underestimate the Southern Ocean carbon sink due to the spatio-temporal distribution of SOCAT data. Our experiments suggest that targeted USV observations could reduce this underestimation of the ocean carbon sink.
Formatted: Subscript
Formatted: Font: Bold, Not Highlight
Formatted: Not Highlight
Formatted: Font: Bold, Not Highlight
Formatted: Font: Bold
Formatted: Font: Bold
Formatted: Highlight
Formatted: Highlight
Formatted: Subscript
Deleted: ¶
Deleted:
Deleted: 2

weakening sink (**Figs. 6d, 9d**). As shown by **Figure 10**, this 'low sink' is significantly exaggerated compared to the 'model truth'. To better understand this discrepancy, we performed an additional experiment based on run 'Z_x10_5Y_YR', but assumed sampling every year for the entire testbed period (i.e., 1982-2016). There is now a significant reduction in the temporal variability of reconstruction bias; with the additional 35-year USV sampling, the reconstructed Southern Ocean air-sea CO_2 flux closely matches the 'model truth' for the entire testbed duration (**Fig. S21**). This suggests that the large decadal variability of air-sea CO_2 fluxes since the 1980s, and the weak anomaly in the Southern Ocean carbon sink in the early 2000s (Le Quéré et al., 2007; Landschützer et al., 2015; Gruber et al., 2019; Bennington et al., 2022a,b; Friedlingstein et al., 2023), may be at least partially attributable to undersampling of the Southern Ocean. This is in agreement with the float sampling experiments performed by Hauck et al. (2023), attributing the strong decadal variability to sparse and skewed SOCAT data distributions. We will further explore this issue in future work. Still, this preliminary experiment suggests that interpretations of trends and variability of the global and Southern Ocean carbon sink should be considered with caution.

Deleted: The results from this experiment show

Deleted: 14

Deleted: 2

5. Conclusions

By using the Large Ensemble Testbed (LET), we show that targeted meridional and winter sampling in the Southern Ocean can improve global and Southern Ocean ML surface ocean pCO_2 reconstructions. Significant improvements are possible by raising the global pCO_2 data density by as little as 0.01-0.07 %. Further, we find that this modest amount of additional Saildrone USV sampling increases the global and Southern Ocean air-sea CO_2 flux by up to 0.1 Pg C yr^{-1}, a quantity equivalent to 25 % of the uncertainty in the ocean carbon sink (0.4 Pg C yr^{-1}; Friedlingstein et al., 2023). Our findings are consistent with previous studies suggesting that additional observations during southern hemisphere winter months and covering meridional gradients can reduce uncertainties and biases in the reconstructions (Lenton et al., 2006; Monteiro et al., 2010; Djeutchouang et al., 2022; Mackay et al., 2022). As opposed to other autonomous platform approaches, Saildrone USVs obtain in situ pCO_2 observations with uncertainties equivalent to the highest-quality observations collected by research ships (± 2 µatm; Sabine et al., 2020; Sutton et al., 2021), and can operate at a high speed so that the spatial extent and seasonal cycle of meridional gradients can be covered. The approach of combining high-accuracy Saildrone USV and SOCAT observations represents thus a promising solution to improve future surface

Deleted: 4

ocean pCO_2 reconstructions and the accuracy of the ocean carbon sink. Lastly, we show that the large variability in bias, and the weakening of the global and Southern Ocean carbon sink in the 2000s, may be partially an artefact of Southern Ocean undersampling.

Code availability

Data analysis scripts will be made available in a GitHub repository upon publication.

Data availability

The Large Ensemble Testbed is publicly available at https://figshare.com/collections/Large_ensemble_pCO2_testbed/4568555.

Author contribution

THH, GAM and AJS designed the experiments, and THH performed the simulations. THH, ARF and LG developed the code. THH and ARF calculated the air-sea fluxes. THH prepared the manuscript with contributions from all co-authors.

Competing interests

The authors declare that they have no conflict of interest.

Acknowledgements

We acknowledge funding from NOAA through the Climate Observations and Monitoring Program (Award #NA20OAR4310340) and from NSF through the LEAP STC (Award #2019625). This is PMEL contribution 5549. We would also like to acknowledge and thank Val Bennington, Julius Busecke, Devan Samant and Abby Shaum for providing technical support, and Viviana Acquaviva for discussions regarding the manuscript. Lastly, we wish to thank two anonymous reviewers, whose contributions greatly improved the manuscript.

Deleted: and

Deleted:

Formatted: Font: 12 pt

Formatted: Highlight

Deleted:

References

Bakker, D. C. E., Pfeil, B., Landa, C. S., Metzl, N., O'Brien, K. M., Olsen, A., Smith, K., Cosca, C., Harasawa, S., Jones, S. D., Nakaoka, S., Nojiri, Y., Schuster, U., Steinhoff, T., Sweeney, C., Takahashi, T., Tilbrook, B., Wada, C., Wanninkhof, R., Alin, S. R., Balestrini, C. F., Barbero, L., Bates, N. R., Bianchi, A. A., Bonou, F., Boutin, J., Bozec, Y., Burger, E. F., Cai, W.-J., Castle, R. D., Chen, L., Chierici, M., Currie, K., Evans, W., Featherstone, C., Feely, R. A., Fransson, A., Goyet, C., Greenwood, N., Gregor, L., Hankin, S., Hardman-Mountford, N. J., Harlay, J., Hauck, J., Hoppema, M., Humphreys, M. P., Hunt, C. W., Huss, B., Ibánhez, J. S. P., Johannessen, T., Keeling, R., Kitidis, V., Körtzinger, A., Kozyr, A., Krasakopoulou, E., Kuwata, A., Landschützer, P., Lauvset, S. K., Lefèvre, N., Lo Monaco, C., Manke, A., Mathis, J. T., Merlivat, L., Millero, F. J., Monteiro, P. M. S., Munro, D. R., Murata, A., Newberger, T., Omar, A. M., Ono, T., Paterson, K., Pearce, D., Pierrot, D., Robbins, L. L., Saito, S., Salisbury, J., Schlitzer, R., Schneider, B., Schweitzer, R., Sieger, R., Skjelvan, I., Sullivan, K. F., Sutherland, S. C., Sutton, A. J., Tadokoro, K., Telszewski, M., Tuma, M., van Heuven, S. M. A. C., Vandemark, D., Ward, B., Watson, A. J., and Xu, S.: A multi-decade record of high-quality $f\mathrm{CO_2}$ data in version 3 of the Surface Ocean CO_2 Atlas (SOCAT), Earth System Science Data, 8, 383–413, https://doi.org/10.5194/essd-8-383-2016, 2016.

Bakker, D. C. E., Alin, S. R., Becker, M., Bittig, H. C., Castaño-Primo, R., Feely, R, A., Gkritzalis, T., Kadono, K., Kozyr, A., Lauvset, S, K., Metzl, N., Munro, D, R., Nakaoka, S., Nojiri, Y., O'Brien, K, M., Olsen, A., Pfeil, Benjamin, P., Denis, S., Tobias, S., Kevin F., Sutton, A. J., Sweeney, C., Tilbrook, B., Wada, C., Wanninkhof, R., Willstrand W. A., Akl, J., Apelthun, L. B., Bates, N., Beatty, C. M., Burger, E. F., Cai, W., Cosca, C. E., Corredor, J. E., Cronin, M., Cross, J. N., De Carlo, E. H., DeGrandpre, M. D., Emerson, S. R., Enright, M. P., Enyo, K., Evans, W., Frangoulis, C., Fransson, A., García-Ibáñez, M. I., Gehrung, M., Giannoudi, L., Glockzin, M., Hales, B., Howden, S. D., Hunt, C. W., Ibánhez, J. S. P., Jones, S. D., Kamb, L., Körtzinger, A., Landa, C. S., Landschützer, P., Lefèvre, N., Lo Monaco, C., Macovei, V. A., Maenner J. S., Meinig, C., Millero, F. J., Monacci, N. M., Mordy, C., Morell, J. M., Murata, A., Musielewicz, S., Neill, ., Newberger, T., Nomura, D., Ohman, M., Ono, T., Passmore, A., Petersen, W., Petihakis, G., Perivoliotis, L., Plueddemann, A. J., Rehder, G., Reynaud, T., Rodriguez, C., Ross, A. C., Rutgersson, A., Sabine, C. L., Salisbury, J. E., Schlitzer, R., Send, U., Skjelvan, I., Stamataki, N., Sutherland, S. C., Sweeney, C., Tadokoro, K., Tanhua, T., Telszewski, M., Trull, T., Vandemark, D., van Ooijen, E., Voynova, Y. G., Wang, H., Weller, R. A., Whitehead, C., Wilson, D.: Surface Ocean CO_2 Atlas Database Version 2022 (SOCATv2022) (NCEI Accession 0253659), NOAA National Centers for Environmental Information [dataset], https://doi.org/10.25921/1h9f-nb73, 2022.

Behncke, J., Landschützer, P. & Tanhua, T. A detectable change in the air-sea CO_2 flux estimate from sailboat measurements. *Scientific Reports*, 14, 3345, https://doi.org/10.1038/s41598-024-53159-0, 2024.

Bennington, V., Galjanic, T., and McKinley, G. A.: Explicit Physical Knowledge in Machine Learning for Ocean Carbon Flux Reconstruction: The pCO_2-Residual Method, Journal of Advances in Modeling Earth Systems, 14(10), https://doi.org/10.1029/2021ms002960, 2022a.

Bennington, V., Gloege, L., and McKinley, G. A.: Variability in the global ocean carbon sink from 1959 to 2020 by correcting models with observations, Geophysical Research Letters, 49(14), https://doi.org/10.1029/2022GL098632, (2022b).

Bushinsky, S. M., Landschützer, P., Rödenbeck, C., Gray, A. R., Baker, D., Mazloff, M. R., Resplandy, L., Johnson, K. S., and Sarmiento, J. L.: Reassessing Southern Ocean air-sea CO_2 flux estimates with the addition of biogeochemical float observations, Global Biogeochemical Cycles, *33*(11), 1370-1388, https://doi.org/10.1029/2019GB006176, 2019.

Chen, T., and Guestrin, C.: Xgboost: A scalable tree boosting system, In: Proceedings of the 22nd ACM SIGKDD international conference on knowledge discovery and data mining (pp. 785-794), https://doi.org/10.1145/2939672.2939785, 2016.

Denvil-Sommer, A., Gehlen, M., and Vrac, M.: Observation system simulation experiments in the Atlantic Ocean for enhanced surface ocean pCO_2 reconstructions, *Ocean Science*, 17, 1011-1030, https://doi.org/10.5194/os-17-1011-2021, 2021.

Deser, C., Phillips. A., Bourdette, V., and Teng. H.: Uncertainty in climate change projections: the role of internal variability, Climate Dynamics, 38, 527-546, https://doi.org/10.1007/s00382-010-0977-x, 2012

Formatted: Font: (Default) Times New Roman, 12 pt

Formatted: Font: (Default) Times New Roman, 12 pt, Not Bold

Formatted: Font: (Default) Times New Roman, 12 pt

Formatted: Font: (Default) Times New Roman, 12 pt

Field Code Changed

Deleted: ¶

Formatted: Font color: Text 1

Formatted: Highlight

Formatted: Subscript, Highlight

Formatted: Highlight

Formatted: Font: Italic, Highlight

Formatted: Highlight

Formatted: Highlight

Formatted: Highlight

Djeutchouang, L. M., Chang, N., Gregor, L., Vichi, M., and Monteiro, P. M. S.: The sensitivity of pCO_2 reconstructions to sampling scales across a Southern Ocean sub-domain: a semi-idealized ocean sampling simulation approach, Biogeosciences, 19, 4171-4195, https://doi.org/10.5194/bg-19-4171-2022, 2022

Fay, A. R., Lovenduski, N. S., McKinley, G. A., Munro, D. R., Sweeney, C., Gray, A. R., Landschützer, P., Stephens, B. B., Takahashi, T., and Williams, N.: Utilizing the Drake Passage Time-series to understand variability and change in subpolar Southern Ocean pCO_2, Biogeosciences, 15(12), 3841-3855, https://doi.org/10.5194/bg-15-3841-2018, 2018.

Fay, A. R., and McKinley, G. A.: Observed regional fluxes to constrain modeled estimates of the ocean carbon sink, Geophysical Research Letters, 48(20), https://doi.org/10.1029/2021GL095325, 2021.

Fay, A. R., Gregor, L., Landschützer, P., McKinley, G. A., Gruber, N., Gehlen, M., Iida, Y., Laruelle, G. G., Rödenbeck, C., Roobaert, A., and Zeng, J.: SeaFlux: harmonization of air-sea CO_2 fluxes from surface pCO_2 data products using a standardized approach, *Earth System Science Data*, 13, 4693-4710, https://doi.org/10.5194/essd-13-4693-2021, 2021.

Friedlingstein, P., O'Sullivan, M., Jones, M. W., Andrew, R. M., Bakker, D. C. E., Hauck, J., Landschützer, P., Le Quéré, C., Luijkx, I. T., Peters, G. P., Peters, W., Pongratz, J., Schwingshackl, C., Sitch, S., Canadell, J. G., Ciais, P., Jackson, R. B., Alin, S. R., Anthoni, P., Barbero, L., Bates, N. R., Becker, M., Bellouin, N., Decharme, B., Bopp, L., Brasika, I. B. M., Cadule, P., Chamberlain, M. A., Chandra, N., Chau, T.-T.-T., Chevallier, F., Chini, L. P., Cronin, M., Dou, X., Enyo, K., Evans, W., Falk, S., Feely, R. A., Feng, L., Ford, D. J., Gasser, T., Ghattas, J., Gkritzalis, T., Grassi, G., Gregor, L., Gruber, N., Gürses, Ö., Harris, I., Hefner, M., Heinke, J., Houghton, R. A., Hurtt, G. C., Iida, Y., Ilyina, T., Jacobson, A. R., Jain, A., Jarníková, T., Jersild, A., Jiang, F., Jin, Z., Joos, F., Kato, E., Keeling, R. F., Kennedy, D., Klein Goldewijk, K., Knauer, J., Korsbakken, J. I., Körtzinger, A., Lan, X., Lefèvre, N., Li, H., Liu, J., Liu, Z., Ma, L., Marland, G., Mayot, N., McGuire, P. C., McKinley, G. A., Meyer, G., Morgan, E. J., Munro, D. R., Nakaoka, S.-I., Niwa, Y., O'Brien, K. M., Olsen, A., Omar, A. M., Ono, T., Paulsen, M., Pierrot, D., Pocock, K., Poulter, B., Powis, C. M., Rehder, G., Resplandy, L., Robertson, E., Rödenbeck, C., Rosan, T. M., Schwinger, J., Séférian, R., Smallman, T. L., Smith, S. M., Sospedra-Alfonso, R., Sun, Q.,

Formatted: Highlight

Formatted: Subscript, Highlight

Formatted: Highlight

Formatted: Subscript, Highlight

Formatted: Highlight

Formatted: Font: Italic, Highlight

Formatted: Font: Italic, Highlight

Formatted: Highlight

Formatted: Font: (Default) Times New Roman, 12 pt, Highlight

Formatted: Font: 12 pt, Highlight

Formatted: Font: (Default) Times New Roman, 12 pt

Sutton, A. J., Sweeney, C., Takao, S., Tans, P. P., Tian, H., Tilbrook, B., Tsujino, H., Tubiello, F., van der Werf, G. R., van Ooijen, E., Wanninkhof, R., Watanabe, M., Wimart-Rousseau, C., Yang, D., Yang, X., Yuan, W., Yue, X., Zaehle, S., Zeng, J., and Zheng, B.: Global Carbon Budget 2023, Earth Syst. Sci. Data, 15, 5301–5369, https://doi.org/10.5194/essd-15-5301-2023, 2023.

Fyfe, J. C., Derksen, C., Mudryk, L., Flato, G. M., Santer, B. D., Swart, N. C., Molotch, N. P., Zhang, X., Wan, H., Arora, V. K., Scinocca, J., and Jiao, Y.: Large near-term projected snowpack loss over the western United States, Nature communications, 8(1), 14996, https://doi.org/10.1038/ncomms14996, 2017.

Gloege, L., McKinley, G. A., Landschützer, P., Fay, A. R., Frolicher, T. L., and Fyfe, J. C.: Quantifying Errors in Observationally Based Estimates of Ocean Carbon Sink Variability, Global Biogeochemical Cycles, 35(4), https://doi.org/10.1029/2020gb006788, 2021.

Gloege, L., Yan, M., Zheng, T. and McKinley, G. A.: Improved quantification of ocean carbon uptake by using machine learning to merge global models and pCO_2 data, Journal of Advances in Modeling Earth Systems, 14(2), https://doi.org/10.1029/2021MS002620, 2022.

Good, S. A., Martin, M., and Rayner, N. A.: EN4: Quality controlled ocean temperature and salinity profiles and monthly objective analyses with uncertainty estimates, Journal of Geophysical Research Oceans, 118(12), 6704-6717, https://doi.org/10.1002/2013JC009067, 2013.

Gray, A. R., Johnson, K. S., Bushinsky, S. M., Riser, S. C., Russell, J. L., Talley, L. D., Wanninkhof, R., Williams, N. L., and Sarmiento, J. L.: Autonomous biogeochemical floats detect significant carbon dioxide outgassing in the high-latitude Southern Ocean, Geophysical Research Letters, 45(17), 9049-9057, https://doi.org/10.1029/2018GL078013, 2018.

Gregor, L., Lebehot, A. D., Kok, S., and Monteiro, P. M. S.: A comparative assessment of the uncertainties of global surface ocean CO_2 estimates using a machine-learning ensemble (CSIR-ML6 version 2019a) – have we hit the wall?, Geoscientific Model Development, 12, 5113-5136, https://doi.org/10.5194/gmd-12-5113-2019, 2019.

Deleted: Friedlingstein, P., Jones, M. W., O'Sullivan, M., Andrew, R. M., Bakker, D. C., Hauck, J., Le Quéré, C., Peters, G. P., Peters, W., Pongratz, J., Sitch, S., Canadell, J. G., Ciais, P., Jackson, R. B., Alin, S. R., Anthoni, P., Bates, N. R., Becker, M., Bellouin, N., Bopp, L., Chau, T. T. T., Chevallier, F., Chini, L. P., Cronin, M., Currie, K. I., Decharme, B., Djeutchouang, L., Dou, X., Evans, W., Feely, R. A., Feng, L., Gasser, T., Gilfillan, D., Gkritzalis, T., Grassi, G., Gregor, L., Gruber, N., Gürses, Ö., Harris, I., Houghton, R. A., Hurtt, C. C., Iida, Y., Ilyina, T., Luijkx, I. T., Jain, A. K., Jones, S. D., Kato, E., Kennedy, D., Goldewijk, K. K., Knauer, J., Korsbakken, J. A., Körtzinger, A., Landschützer, P., Lauvset, S. K., Lefèvre, N., Lienert, S., Liu, J., Marland, G., McGuire, P. C., Melton, J. R., Munro, D. R., Nabel, J. E. M. S., Nakaoka, S-I., Niwa, Y., Ono, T., Pierrot, D., Poulter, B., Rehder, G., Resplandy, L., Robertson, E., Rödenbeck, C., Rosan, T. M., Schwinger, J., Schwingshackl, C., Séférian, R., Sutton, A. J., Sweeney, C., Tanhua, T., Tans, P. P., Tian, H., Tilbrook, B., Tubiello, F., Werf, G. V. D., Vuichard, N., Wada, C., Wanninkhof, R., Watson, A., Willis, D., Wiltshire, A. J., Yuan, W., Yue, C., Yue, X., Zaehle, S., and Zeng, J.: Global carbon budget 2021, Earth System Science Data, 14(4), 1917-2005, https://doi.org/10.5194/essd-14-1917-2022, 2022

Gregor, L. and Fay, A. R.: Air-sea CO_2 fluxes for surface pCO_2 data products using a standardized approach, Zenodo [code], https://doi.org/10.5281/zenodo.5482547, 2021.

Gruber, N., Landschützer, P., and Lovenduski, N. S.: The variable Southern Ocean carbon sink, The Annual Review of Marine Science, 11, 159-86, https://doi.org/10.1146/annurev-marine-121916-063407, 2019.

Hauck, J., Nissen, C., Landschützer, P., Rödenbeck, C., Bushinsky, S., and Olsen, A.: Sparse observations induce large biases in estimates of the global ocean CO2 sink: and ocean model subsampling experiment, Philosophical Transactions Of the Royal Society A, 381:20220063, https://doi.org/10.1098/rsta.2022.0063, 2023.

Kay, J. E., Deser, C., Phillips, A., Mai, A., Hannay, C., Strand, G., Arblaster, J. M., Bates, S. C., Danabasoglu, G., Edwards, J., Holland, M., Kuschner, P., Lamarque, J-F., Lawrence, D., Lindsay, K., Middelton, A., Munoz, E., Nealse, R., Oleson, K., Polvani, L., and Vertenstein, M.: The Community Earth System Model (CESM) large ensemble project: A community resource for studying climate change in the presence of internal climate variability, Bulletin of the American Meteorological Society, 96(8), 1333-1349, https://doi.org/10.1175/BAMS-D-13-00255, 2015.

Khatiwala, S., Primeau, F., and Hall., T.: Reconstruction of the history of anthropogenic CO2 concentrations in the ocean, Nature, 462(7271), 346-349, https://doi.org/10.1038/nature08526, 2009.

Landschützer, P., Gruber, N., Bakker, D. C. E., and Schuster, U.: Recent variability of the global ocean carbon sink, Global Biogeochemical Cycles, 28(9), 927-949, https://doi.org/10.1002/2014GB004853, 2014.

Landschützer, P., Gruber, N., Haumann, F. A., Rödenbeck, C., Bakker, D. C. E., Van Heuven, S., Hoppema, M., Metzl, N., Sweeney, C., Takahashi, T., Brook, B., and Wanninkhof, R.: The reinvigoration of the Southern Ocean carbon sink, Science, 349(6253), 1221-1224, https://doi.org/10.1126/science.aab2620, 2015.

Landschützer, P., Tanhua, T., Behncke, J., and Keppler, L.: Sailing through the Southern Ocean seas of air-sea CO_2 flux uncertainty, Philosophical Transactions of the Royal Society A, 381, https://doi.org/10.1098/rsta.2022.0064, 2023.

Formatted: Font: 12 pt

Formatted: Font: 12 pt

Deleted: .

Lenton, A. B., Matear, R. J., and Tilbrook, B.: Design of an observational strategy for quantifying the Southern Ocean uptake of CO_2, Global Biogeochemical Cycles, 20, 1-11. https://doi.org/10.1029/2005GB002620, 2006.

Lenton, A. B., Tilbrook, B., Law, R. M., Bakker, D. C. E., Doney, S. C., Gruber, N., Ishii, M., Hoppema, M., Lovenduski, N. S., Matear, R. J., McNeil. B. I., Metzl, N., Mikaloff Fletcher, S. E., Monteiro, P. M. S., Rödenbeck, C., Sweeney, C., and Takahashi, T.: Sea-air CO_2 fluxes in the Southern Ocean for the period 1990-2009, Biogeosciences, 10, 4037-4054, https://doi.org/10.5194/bg-10-4037-2013, 2013.

Le Quéré, C., Rödenbeck, C., Buitenhuis, E. T., Conway, T. J., Lagenfelds, R., Gomez, A., Labuschagne C., Ramonet, M., Nakazawa, T., Metzl, N., Gillett, N., and Heimann, M.: Saturation of the Southern Ocean CO2 sink due to recent climate change, Science, 316(5832), 1735-1738, https://doi.org/10.1126/science.1136188, 2007.

Long, M. C., Stephens, B. B., McKain, K., Sweeney, C., Keeling, R. F., Kort, E. A., Morgan, E. J., Bent, J. D., Chandra, N., Chevallier, F., Commane, R., Daube, B. C., Krummel, P. B., Loh, Z., Luijkx, I. T., Munro, D., Patra, P., Peters, W., Ramonet, M., Rödenbeck, C., Stavert, A., Tans, P., and Wofsy, S. C.: Strong Southern Ocean carbon uptake evident in airborne observations, Science, 374(6572), 1275-1280, https://doi.org/10.1126/science.abi4355, 2021.

Mackay, N., and Watson, A.: Winter air-sea CO_2 fluxes constructed from summer observations of the polar Southern Ocean suggest weak outgassing, Journal of Geophysical Research: Oceans, 126(5), e2020JC016600, https://doi.org/10.1029/2020JC016600, 2021.

Mackay, N., Watson, A., Suntharalingam, P., Chen, Z., and Rödenbeck, C.: Improved winter data coverage of the Southern Ocean CO_2 sink from extrapolation of summertime observations, Communications Earth & Environment, 3, 265, https://doi.org/10.1038/s43247-022-00592-6, 2022.

McKinley, G. A., Fay, A. R., Eddebbar, Y. A., Gloege, L., and Lovenduski, N. S.: External forcing explains recent decadal variability of the ocean carbon sink, AGU Advances, 1(2), e2019AV000149, https://doi.org/10.1029/2019AV000149, 2020.

Mongwe, N. P., Vichi, M., and Monteiro, P. M. S.: The seasonal cycle of $p$$CO_2$ and CO_2 fluxes in the Southern Ocean: diagnosing anomalies in CMIP5 Earth system models, Biogeosciences, 15(9), 2851-2872, https://doi.org/10.5194/bg-15-2851-2018, 2018.

Monteiro, P. M. S., Gregor, L., Lévy, M., Maenner, S., Sabine, C. L., and Swart, S.: Intraseasonal variability linked to sampling alias in air-sea CO_2 fluxes in the Southern Ocean, Geophysical Research Letters, 42(20), 8507-8514, https://doi.org/10.1002/2015GL066009, 2015.

Rodgers, K. B., Lin, J., and Frölicher, T. L.: Emergence of multiple ocean ecosystem drivers in a large ensemble suite with an Earth system model, Biogeosciences, 12(11), 3301-3320. https://doi.org/10.5194/bg-12-3301-2015, 2015.

Rödenbeck, C., Bakker, D. C. E., Gruber, N., Iida, Y., Jacobson, A. R., Jones, S., Landschützer, P., Metzl, N., Nakaoka, S., Olsen, A., Park, G.-H., Peylin, P., Rodgers, K. B., Sasse T. P., Schuster, U., Shutler, J. D., Valsala, V., Wannikkhof, R., and Zeng, J.: Data-based estimates of the ocean carbon sink variability – first results of the Surface Ocean $p$$CO_2$ Mapping intercomparison (SOCOM), Biogeosciences, 12, 7251-7278, https://doi.org/10.5194/bg-12-7251-2015, 2015.

Sabine, C., Sutton, A., McCabe, K., Lawrence-Slavas, N., Alin, S, Feely, R., Jenkins, R., Maenner, S., Meinig, C., Thomas, J., van Ooijen, E., Passmore, A., and Tilbrook, B.: Evaluation of a new carbon dioxide system for autonomous surface vehicles, Journal of Atmospheric and Oceaenic Technology, 37(8), 1305-1317, https://doi.org/10.1175/JTECH-D-20-0010.1, 2020.

Stamell, J., Rustagi, R. R., Gloege, L., and McKinley, G. A.: Strengths and weaknesses of three Machine Learning methods for pCO_2 interpolation, Geoscientific Model Development Discussions[preprint], doi:10.5194/gmd-2020-311, 22 October 2020.

Sutton, A. J., Williams, N. L., and Tilbrook, B.: Constraining Southern Ocean CO_2 flux uncertainty using uncrewed surface vehicle observations, Geophysical Research Letters, 48(3), e2020GL091748, https://doi.org/10.1029/2020GL091748, 2021.

Takahashi, T., Olafsson, J., Goddard, J. G., Chipman, D. W., and Sutherland, S. C.: Seasonal variation of CO2 and nutrients in the high-latitude surface oceans: A comparative study, Global Biogeochemical Cycles, 7(4), 843-878, https://doi.org/10.1029/93GB02263, 1993.

Deleted: .

Deleted: ¶

Takahashi, T., Sutherland, S. C., Wanninkhof, R., Sweeney, C., Feely, R. A., Chipman, D. W., Hales, B., Friederich, G., Chavez, F., Sabine, C., Watson, A., Bakker, D. C. E., Schuster, U., Metzl, N., Yoshikawa-Inoue, H., Ishii, M., Midorikawa, T., Nojiri, Y., Körtzinger, A., Steinhoff, T., Hoppema, M., Olafsson, J., Arnarson, T. S., Tilbrook, B., Johannessen, T., Olsen, A., Bellerby, R., Wong, C. S., Delille, B., Bates, N. R., and de Baar, H. J. W.: Climatological mean and decadal change in surface ocean pCO_2, and net sea-air CO_2 flux over the global oceans, Deep Sea Research Part II: Topical Studies in Oceanography, 56(8-10), 554-557, https://doi.org/10.1016/j.dsr2.2008.12.009, 2009.

Toms, B. A., Barnes, E. A., and Ebert-Uphoff, I.: Physically interpretable neural networks for the geosciences: Applications to earth system variability, Journal of Advances in Modeling Earth Systems, 12(9), e2019MS002002, https://doi.org/10.1029/2019MS002002, 2020.

Wanninkhof, R.: Relationship between wind speed and gas exchange over the ocean revisited, *Limnology and Oceanography: Methods*, 12, 351-362, https://doi.org/10.4319/lom.2014.12.351, 2014.

Williams, N. L., Juranek, L. W., Feely, R. A., Johnson, K. S., Sarmiento, J. L., Talley, L. D., Dickson, A. G., Gray, A. R., Wannikhof, R., Russell, J. L., Riser, S. C., and Takeshita, Y.: Calculating surface ocean pCO_2 from biogeochemical Argo floats equipped with pH: An uncertainty analysis, Global Biogeochemical Cycles, 31(3), 591-604, https://doi.org/10.1002/2016GB005541, 2017.

Wu, Y., Bakker, D. C. E., Achterberg, E. P., Silva, A. N., Pickup D. P., Li, X., Hartman, S., Stappard, D., Qi, D., and Tyrrell, T.: Integrated analysis of carbon dioxide and oxygen concentrations as a quality control of ocean float data, Communications Earth & Environment, 3, 92, https://doi.org/10.1038/s43247-022-00421-w, 2022.

Formatted: Highlight

Formatted: Font: Italic, Highlight

Formatted: Highlight

Formatted: Font: (Default) Times New Roman, 12 pt, Not Bold, Highlight

Formatted: Highlight

Formatted: Not Highlight

Page 19: [1] Deleted	Thea Hatlen Heimdal	12/14/23 4:52:00 PM

Page 19: [1] Deleted	Thea Hatlen Heimdal	12/14/23 4:52:00 PM

Page 19: [1] Deleted	Thea Hatlen Heimdal	12/14/23 4:52:00 PM

Page 19: [1] Deleted	Thea Hatlen Heimdal	12/14/23 4:52:00 PM

Page 19: [1] Deleted	Thea Hatlen Heimdal	12/14/23 4:52:00 PM

Page 19: [1] Deleted	Thea Hatlen Heimdal	12/14/23 4:52:00 PM

Page 19: [1] Deleted	Thea Hatlen Heimdal	12/14/23 4:52:00 PM

Page 19: [1] Deleted	Thea Hatlen Heimdal	12/14/23 4:52:00 PM

Page 19: [1] Deleted	Thea Hatlen Heimdal	12/14/23 4:52:00 PM

Page 19: [1] Deleted	Thea Hatlen Heimdal	12/14/23 4:52:00 PM

Page 19: [1] Deleted	Thea Hatlen Heimdal	12/14/23 4:52:00 PM

Page 23: [2] Deleted	Thea Hatlen Heimdal	11/27/23 2:39:00 PM

Page 23: [2] Deleted Thea Hatlen Heimdal 11/27/23 2:39:00 PM

Page 23: [2] Deleted Thea Hatlen Heimdal 11/27/23 2:39:00 PM

Page 23: [2] Deleted Thea Hatlen Heimdal 11/27/23 2:39:00 PM

Page 23: [2] Deleted Thea Hatlen Heimdal 11/27/23 2:39:00 PM

Page 23: [2] Deleted Thea Hatlen Heimdal 11/27/23 2:39:00 PM

Page 23: [2] Deleted Thea Hatlen Heimdal 11/27/23 2:39:00 PM

Page 23: [2] Deleted Thea Hatlen Heimdal 11/27/23 2:39:00 PM

Page 23: [2] Deleted Thea Hatlen Heimdal 11/27/23 2:39:00 PM

Page 23: [2] Deleted Thea Hatlen Heimdal 11/27/23 2:39:00 PM